Deterministic radiative transfer equation solver on unstructured tetrahedral meshes: Efficient assembly and preconditioning

Pierre Jolivet, Mohd Afeef Badri, Y. Favennec

Version of Record: https://www.sciencedirect.com/science/article/pii/S0021999121002084
Manuscript_a6faf2282f25d7df14fa4af329227341

Deterministic Radiative Transfer Equation Solver on Unstructured Tetrahedral Meshes: Efficient Assembly and Preconditioning

P. Jolivet[a,*], M. A. Badri[b], Y. Favennec[c]

[a] *CNRS, Institut de Recherche en Informatique de Toulouse, 31062 Toulouse, France*
[b] *Université Paris-Saclay, CEA, Service de Thermo-hydraulique et de Mécanique des Fluides, 91191 Gif-sur-Yvette, France*
[c] *CNRS, Laboratoire de Thermique et Énergie de Nantes, 44306 Nantes, France*

Abstract

Due to its integro-differential nature, deriving schemes for numerically solving the radiative transfer equation (RTE) is challenging. Most solvers are efficient in specific scenarios: structured grids, simulations with low-scattering materials... In this paper, a full solver, from the discretization of the steady-state monochromatic RTE to the solution of the resulting system, is derived.

Using a mixed matrix-ready/matrix-free approach, our solver is able to discretize and solve a 45.7 billion unknown problem on 27 thousand processes in three minutes for a full physics involving scattering, absorption, and reflection. Because of the high dimensionality of the continuous equation, the linear system would have had more than 6×10^{15} nonzero entries if assembled explicitly. Our approach allows for large memory gains by only storing lower dimension reference matrices.

The finite element-based solver is wrapped around open-source software, FreeFEM for discretization, PETSc for linear algebra, and *hypre* for the algebraic multigrid infrastructure. Overall, deterministic results are presented on arbitrarily-decomposed unstructured grids for radiative transfer problems with scattering, absorbing, and reflecting heterogeneities on up to 27 thousand processes.

Keywords: radiative transfer, matrix-free solver, algebraic multigrid

1. Introduction

Radiative transfer is the phenomenon of energy transfer in the form of electromagnetic radiation, often characterized by its radiative intensity I. This intensity within any participating medium is affected by absorption, emission, reflection, and scattering processes. The radiative transfer equation (RTE) models such processes at the continuous level. The RTE is commonly used in the fields of thermal radiation [1, 2], neutronics [3, 4], astrophysics [5, 6], and optical imaging [7, 8], to name a few. This equation, in its steady-state monochromatic form, is stated as the following integro-differential equation:

$$(\vec{s} \cdot \nabla + \beta(\vec{x}))\, I(\vec{x}, \vec{s}) = \sigma(\vec{x}) \oint_{\mathcal{S}} I(\vec{x}, \vec{s}\,')\phi(\vec{s}, \vec{s}\,')\mathrm{d}\vec{s}\,' + \kappa(\vec{x}) I_b(\vec{x}), \tag{1}$$

where $\vec{x} = (x, y, z) \in \Omega \subset \mathbb{R}^3$ and $\mathrm{d}\vec{s}$ is the differential solid angle around the direction $\vec{s} = [\cos\varphi \sin\theta, \sin\varphi \sin\theta, \cos\theta]^T$, $(\varphi, \theta) \in [0, 2\pi] \times [0, \pi]$ being the azimuthal and the zenith angles, respectively. β is the extinction coefficient computed as the sum $\kappa + \sigma$, where κ (resp. σ) is the absorption (resp. scattering) coefficient. These three coefficients are piecewise constant in Ω and their values depend on the various participating media in the domain. ϕ is a scattering phase function that quantifies the probability of a photon traveling in $\vec{s}\,'$ being scattered towards $\vec{s}$. Finally, I_b is the radiation from a black body specified by Planck's law.

Efficient solution strategy for the monochromatic steady-state RTE is still an active area of research for cases that involve scattering and reflections in complex geometries [9, 10]. The main challenge, for methods presented in this article, is the presence of in-scattering from the surface integral in eq. (1), which leads to coupled systems that are difficult to solve due to memory and convergence issues. Associated with the multigroup approximation [11, 12] or spectral models [13, 14], monochromatic RTE solvers are a stepping stone for designing multi-frequency RTE solvers in different scientific communities, e.g., combustion [15, 16].

In most of this paper, the boundary $\partial\Omega$ is assumed to be nonreflective. If $\vec{n}$ is the outward normal vector at a given point of $\partial\Omega$, the following inflow boundary condition is used to provide closure to eq. (1):

$$I = I_{\text{inflow}} \quad \forall (\vec{x}, \vec{s}) \in \Gamma^- = \{(\vec{x}, \vec{s}) : \vec{x} \in \partial\Omega, \vec{s} \cdot \vec{n} < 0\}. \tag{2}$$

*Corresponding author: pierre.jolivet@enseeiht.fr

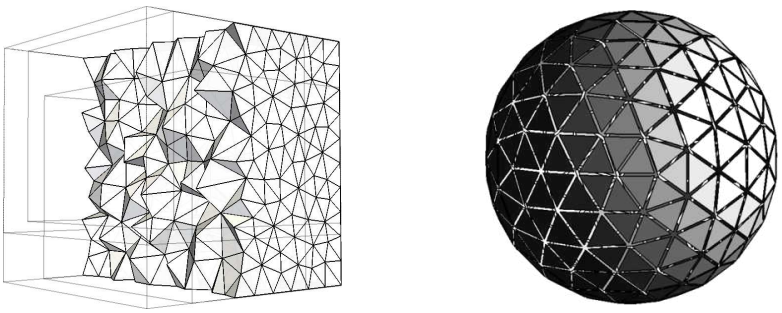

(a) Spatial mesh. (b) Angular mesh ($N_d = 320$).

Figure 1: DOM and FEM coupling strategy, each spatial unknown is associated with a set of N_d angular unknowns.

One needs two schemes for discretizing eq. (1) both in space $\vec{x}$ and angles $\vec{s}$. In this work, we couple the finite element method (FEM) for the spatial discretization with the discrete ordinates method (DOM) based on the sphere triangulation for the angular discretization [17, 18]. The terminology DOM is used throughout the paper.

Angular discretization. The DOM, here performed according to the unit sphere triangulation, either based on Thurgood's method [19] or icosahedron refinements [5], cf. fig. 1b, provides a set of directions and weights $\{(\vec{s}_k, \omega_k)\}_{k=1}^{N_d}$. Such a scheme is second-order accurate when combined with piecewise linear finite elements in space [20]. The continuous intensity is now approximated by a set of discrete intensities $\{I_k\}_{k=1}^{N_d}$. The surface integral in eq. (1) is thus evaluated as, for all discrete directions $k \in [\![1; N_d]\!]$:

$$\oint_{\mathcal{S}} I(\vec{x}, \vec{s})\phi(\vec{s}_k, \vec{s})\mathrm{d}\vec{s} \approx \sum_{j=1}^{N_d} \omega_j I_j(\vec{x})\phi_{k,j}.$$

The integro-differential eq. (1) may now be stated as a set of N_d continuous partial differential equations:

$$\forall k \in [\![1; N_d]\!], (\vec{s}_k \cdot \nabla + \beta(\vec{x}))I_k(\vec{x}) = \sigma(\vec{x}) \sum_{j=1}^{N_d} \omega_j I_j(\vec{x})\phi_{k,j} + \kappa(\vec{x})I_b(\vec{x}). \tag{3}$$

In a similar fashion the inflow boundary condition from eq. (2) has to be rewritten in discrete angular form. In this paper, collimated beams of intensity I_{inflow} impinge the boundary along prescribed entrant directions in $L \subset [\![1; N_d]\!]$. Hence, $\forall k \in [\![1; N_d]\!]$:

$$I_k = \begin{cases} I_{\text{inflow}} & \forall \vec{x} \in \partial\Omega : \vec{s}_k \cdot \vec{n} < 0, \text{ if } k \in L, \\ 0 & \text{otherwise.} \end{cases} \tag{4}$$

Spatial discretization. With the FEM, given a spatial mesh Ω^h, cf. fig. 1a, and a set of appropriate functional spaces $\{\mathcal{V}_k^h\}_{k=1}^{N_d}$, the following variational equations may be defined using the Galerkin method. The finite element trial functions for the discrete radiative intensities $\{I_k^h \in \mathcal{V}_k^h\}_{k=1}^{N_d}$ have to satisfy for all test functions $\{J_k^h \in \mathcal{V}_k^h\}_{k=1}^{N_d}$:

$$\forall k \in [\![1; N_d]\!], \int_{\Omega^h} \left((\vec{s}_k \cdot \nabla + \beta(\vec{x}))I_k^h(\vec{x}) - \sigma(\vec{x}) \sum_{j=1}^{N_d} \omega_j I_j^h(\vec{x})\phi_{k,j} \right) J_k^h(\vec{x})\mathrm{d}\vec{x} = \int_{\Omega^h} \kappa(\vec{x})I_b(\vec{x})J_k^h(\vec{x})\mathrm{d}\vec{x},$$

with the boundary conditions defined in eq. (4). In this paper, it is assumed that for all directions, the same functional space $\mathcal{V}^h$ is used to search for all the discrete radiative intensities, i.e., for all k in $[\![1; N_d]\!]$, $\mathcal{V}_k^h = \mathcal{V}^h$. In particular, $\mathcal{V}^h$ is the space of piecewise linear functions throughout the paper. Because of the convection-dominant term in eq. (1), an artificial diffusivity is introduced, and the following test functions derived from the SUPG method [21] are used: $J_k^h + \gamma\vec{s}_k \cdot \nabla J_k^h$. An effective piecewise constant value of γ was determined in prior works [22]: $\gamma(\vec{x}) = \left(\frac{4}{h^2} + \beta(\vec{x})^2 + \frac{4\sigma(\vec{x})}{hN_d} \right)^{-1/2}$, where h is the size of each spatial element. By integrating

by parts, the system of variational formulations becomes: $\forall k \in [\![1; N_d]\!]$,

$$\begin{aligned}\int_{\Omega^h} \Bigg(\Big(\beta(\vec{x}) I_k^h(\vec{x}) - \sigma(\vec{x}) \sum_{j=1}^{N_d} \omega_j I_j^h(\vec{x}) \phi_{k,j}\Big) \left(J_k^h(\vec{x}) + \gamma(\vec{x}) \vec{s}_k \cdot \nabla J_k^h(\vec{x})\right) \\ - \left(\vec{s}_k \cdot \nabla J_k^h(\vec{x})\right) I_k^h(\vec{x}) + \gamma(\vec{x}) \left(\vec{s}_k \cdot \nabla I_k^h(\vec{x})\right) \left(\vec{s}_k \cdot \nabla J_k^h(\vec{x})\right) \Bigg) \mathrm{d}\vec{x} \\ = \int_{\Omega^h} \kappa(\vec{x}) I_b(\vec{x}) \left(J_k^h(\vec{x}) + \gamma(\vec{x}) \vec{s}_k \cdot \nabla J_k^h(\vec{x})\right) \mathrm{d}\vec{x} \\ - \int_{\Gamma^-} \vec{s}_k \cdot \vec{n}\ J_k^h(\vec{x}) I_{\text{inflow}}(\vec{x}) \mathrm{d}\vec{x} - \int_{\partial\Omega^h \setminus \Gamma^-} \vec{s}_k \cdot \vec{n}\ I_k^h(\vec{x}) J_k^h(\vec{x}) \mathrm{d}\vec{x}.\end{aligned} \tag{5}$$

Now that the RTE has been discretized both in space and angles, it is possible to highlight the major contributions of this paper. Indeed, we present:

- an efficient way to assemble linear systems arising from the discretization of eq. (5),
- a scalable approach for solving such linear systems using a mixed matrix-ready/matrix-free approach,
- how to handle physics involving specular reflections.

The paper is organized as follows. In section 2, related work and limitations of current implementations of radiative transfer equation solvers are presented. In section 3, the flexibility of modern finite element domain specific languages is leveraged to efficiently discretize eq. (5) numerically. In section 4, methods to iteratively solve the large systems generated in the previous section on thousands of processes are presented. Validation and scaling analysis of our solver is presented in section 5. The capabilities of our solver when dealing with specular reflections are shown in section 6.

2. Related work

Most RTE solvers are either physics-based (stochastic) or deterministic. Concerning the former, Monte Carlo [23] or ray-tracing methods [24] are well-suited to parallel computing [25]. However, computations involving optically thick media are numerically challenging for such methods [26]. Moreover, coupling these with other physics, e.g., fluid mechanics, is also demanding [27].

For deterministic solvers, historically, the surface integral from eq. (1) was dealt with by the introduction of the DOM [28]. Though new approaches for discretizing in angles exist [29], it is still nowadays the most used technique for semi-discretizing the integro-differential RTE into a set of coupled PDEs on which standard spatial discretization schemes are applicable. In the field of radiative transfer, the DOM is often combined with the finite volume method (FVM) [1].

As an alternative, one may also use the FEM. Many recent works in the radiative transfer community support its use together with the DOM to improve the efficiency of radiative transport equation solvers [5, 30, 31, 9], or to deal with complex geometries [32, 33] or coupled physics [2].

Regardless of the spatial discretization, the fully discrete set of linear equations is commonly solved by a direction-by-direction iterative scheme known as source iteration [34, 35, 36]. It provides a memory-efficient strategy needed to handle the high-dimensionality of RTE in its discrete form eq. (5). Then, an optimal sweeping sequence is performed to compute solution of linear systems. Source iteration is widely popular in parallel deterministic solvers: Uintah [37] from University of Utah, Denvo [38] from ORNL, Ardra [39] from LLNL, PDT [40] from TAMU. However, they are most often optimized for regular geometries that have to be (semi-)structurally meshed to facilitate optimal marching (sweeping sequence) [41], which is also sensitive to boundary conditions, unless, e.g., orthogonality conditions between reflective surfaces hold [42]. These schemes may be extended to unstructured grids [43, 44, 45, 46, 47] but with understandably lower parallel efficiencies.

Krylov methods have been often used with source iteration. They are particularly suited to situations where there is a tight coupling between the discrete directions, e.g., strongly scattering or reflecting media [48]. Currently, there are different ways to leverage Krylov methods for solving the discrete RTE, e.g.:

- direct application on the full linear system yielded by the spatial and DOM discretizations [49];
- in conjunction with sweep-based iterative schemes recasted as preconditioned operators [50].

The latter choice is often less memory-demanding since the workload can be implemented direction-by-direction. Contrary to direction-by-direction schemes, all the discrete radiative intensities are considered simultaneously in the present work. Consequently, RTE solvers based on direct application of Krylov methods are most often limited by the high dimensionality of eq. (5) and thus require a large amount of memory to store the according

linear system. As such, these solvers usually tackle small-scale problems [51, 49] (up to 512 MPI processes on a regularly-decomposed Cartesian grid of 262 thousand elements with up to 120 directions) [52] (up to four directions in 2D) or have to rely on tools such as adaptive mesh refinement in space [53] or in angles [54], which may complexify a distributed solver due to the need of proper load balance. To deal with larger problems, at least two modern ways to solve the RTE have emerged. First, the use of reduced order models [55] or sparse grids may be used to deal efficiently with the "curse of dimensionality" [56, 57] (up to $3 \cdot 10^6$ unknowns solved sequentially). Second, Jacobian-free Newton–Krylov methods [58] have been extended to the RTE [59] (up to 512 MPI processes and 8 threads per MPI process on a Cartesian grid of 65 thousand elements with up to 120 directions). These two methods are based on simplifications of the RTE by approximating either the interactions between the unknowns in space and in angles for the latter, or the global operator for the former.

3. Efficient assembly

Nowadays, the finite element method is available in a large number of professional or academic domain specific (embedded) languages: deal.II [60], FEniCS [61], FreeFEM [62], etc. The goal of the next section is to show that these software typically cannot cope with the dimension complexity of the RTE if the corresponding linear system is assembled explicitly. However, we will use one of them, FreeFEM, to discretize auxiliary problems and show how this relates to the original PDE.

3.1. Vectorial finite elements

Naively, N_d linear systems need to be assembled corresponding to the N_d variational formulations of eq. (5). However, by introducing the vectorial finite element space $\mathbb{V}^h$ defined as the Cartesian product of N_d finite element spaces $\mathcal{V}^h$, eq. (5) may be formulated in terms of a single vectorial unknown $\mathbb{I}^h$ and a single vectorial test function $\mathbb{J}^h$. Let $\mathbb{I}^h = [I_1^h \cdots I_{N_d}^h]^T$, $\mathbb{J}^h = [J_1^h \cdots J_{N_d}^h]^T$, $\mathbb{S} = [\vec{s}_1 \cdots \vec{s}_{N_d}]^T$, and $\{\Phi_{i,j} = \omega_j \phi_{i,j}\}_{i,j=1}^{N_d}$. If we denote by $\otimes$ (resp. $\odot$) the entrywise product (resp. scalar product) of two vectorial functions, and by $\diamond$ the product of a matrix by a vectorial function, then, the bilinear part of eq. (5) becomes, for all $\mathbb{J}^h \in \mathbb{V}^h$:

$$
\begin{aligned}
a(\mathbb{I}^h, \mathbb{J}^h) = \int_{\Omega^h} \Big(\big(\beta(\vec{x})\mathbb{I}^h(\vec{x}) - \sigma(\vec{x})\Phi \diamond \mathbb{I}^h(\vec{x})\big) \otimes \big(\mathbb{J}^h(\vec{x}) + \gamma(\vec{x})\mathbb{S} \odot \nabla \mathbb{J}^h(\vec{x})\big) \\
+ \gamma(\vec{x})\big(\mathbb{S} \odot \nabla \mathbb{I}^h(\vec{x})\big) \otimes \big(\mathbb{S} \odot \nabla \mathbb{J}^h(\vec{x})\big) - \big(\mathbb{S} \odot \nabla \mathbb{J}^h(\vec{x})\big) \otimes \mathbb{I}^h(\vec{x}) \Big) \mathrm{d}\vec{x} \\
+ \int_{\partial\Omega^h \setminus \Gamma^-} \Big(\big(\mathbb{S} \odot \vec{n}\big) \otimes \mathbb{J}^h(\vec{x}) \Big) \otimes \mathbb{I}^h(\vec{x}) \mathrm{d}\vec{x}.
\end{aligned}
\tag{6}
$$

The same goes for the linear part of eq. (5) such that one may write for all $\mathbb{J}^h \in \mathbb{V}^h$: $a(\mathbb{I}^h, \mathbb{J}^h) = l(\mathbb{J}^h)$.

3.2. Matrix-ready assembly

Let the linear system yielded by the discretization of the previous equation be written as:

$$
\mathbb{A}\mathbb{X} = \mathbb{B}. \tag{7}
$$

If the number of degrees of freedom in $\mathcal{V}^h$ is n, since the number of components in the vectorial finite element space $\mathbb{V}^h$ is equal to the number of directions N_d in the angular mesh, $\mathbb{A}$ is of order $N_d \cdot n$. Furthermore, if it is assumed that each component of $\mathbb{V}^h$ is interleaved in $\mathbb{A}$, $\mathbb{X}$, and $\mathbb{B}$, then:

- the sparse matrix $\mathbb{A}$ is made of dense $N_d \times N_d$ blocks,
- $\mathbb{B} = [b_{1,1}, \ldots, b_{N_d,1}, b_{1,2}, \ldots, b_{N_d,2}, \ldots, b_{1,n}, \ldots, b_{N_d,n}]^T$.

Increasing the number of directions for the DOM means that the number of nonzero coefficients in $\mathbb{A}$ will increase as well. In practice, the efficiency of two traditional finite element languages, FEniCS and FreeFEM, is assessed in fig. 2. For this test case, the RTE is discretized in a unit two-dimensional square using a fixed unstructured spatial mesh made of 6,768 triangles. The resulting finite element space $\mathcal{V}^h$ has 3,487 degrees of freedom. The time spent to assemble the corresponding linear systems, while increasing the number of directions N_d, is displayed. The results have been averaged over five consecutive runs, performed after cache warming. With FEniCS, prior to any computations, a first run to JIT compile the solver is also performed. This is done in sequential, on a single core of an Intel Core i7-6567U. Clearly, these timings are not satisfactory since both the spatial and angular meshes are tiny. They could not be used to resolve any nontrivial physics.

3.3. Semi-matrix-free assembly

The two previous general-purpose languages do not succeed at exploiting the structure of eq. (6). Instead, they assemble the matrix from eq. (7) coefficient by coefficient, which has thus a cost proportional to the order of the linear system $N_d \cdot n$. If it is assumed that the sparse matrix $\mathbb{A}$ does not have to be assembled explicitly, this cost may be greatly reduced. Indeed, if one looks for example at the following term from the bilinear form eq. (6): $\int_{\Omega^h} \beta(\vec{x}) \mathbb{I}^h(\vec{x}) \otimes \mathbb{J}^h(\vec{x}) \mathrm{d}\vec{x}$, assembled as $\mathbb{A}_1$, one can instead discretize this bilinear form $\int_{\Omega^h} \beta(\vec{x}) I^h(\vec{x}) J^h(\vec{x}) \mathrm{d}\vec{x}$, assembled as $\mathcal{A}_1$, where both I^h and J^h are in the finite element space $\mathcal{V}^h$ (of dimension n), and not in $\mathbb{V}^h$ (of dimension $N_d \cdot n$). The action of $\mathbb{A}_1$ on a vector $\mathbb{X}$ of order $N_d \cdot n$, is nothing else than the action of $\mathcal{A}_1$ on all N_d components of order n of $\mathbb{X}$: $\forall (k,i) \in [\![1; N_d]\!] \times [\![1; n]\!]$,

$$(\mathbb{A}_1 \mathbb{X})_{k+N_d \cdot (i-1)} = \left(\mathcal{A}_1 [x_{k,1} \cdots x_{k,n}]^T\right)_i .$$

Now, looking at:

$$\begin{aligned} a_2(\mathbb{I}^h, \mathbb{J}^h) &= \int_{\Omega^h} \Big(\big(\beta(\vec{x}) \mathbb{I}^h(\vec{x})\big) \otimes \big(\gamma(\vec{x}) \mathbb{S} \odot \nabla \mathbb{J}^h(\vec{x})\big) - \big(\mathbb{S} \odot \nabla \mathbb{J}^h(\vec{x})\big) \otimes \mathbb{I}^h(\vec{x}) \Big) \mathrm{d}\vec{x} \\ &= \int_{\Omega^h} \big((\gamma(\vec{x})\beta(\vec{x}) - 1) \mathbb{I}^h(\vec{x})\big) \otimes \big(\mathbb{S} \odot \nabla \mathbb{J}^h(\vec{x})\big) \, \mathrm{d}\vec{x}, \end{aligned}$$

assembled as $\mathbb{A}_2$, it is instead possible to assemble the operators $\mathcal{A}_{2a}, \mathcal{A}_{2b}$, and $\mathcal{A}_{2c}$, corresponding to the discretization of the following bilinear forms:

$$\begin{aligned} a_{2a}(I^h, J^h) &= \int_{\Omega^h} (\gamma(\vec{x})\beta(\vec{x}) - 1) I^h(\vec{x}) \frac{\partial J^h(\vec{x})}{\partial x} \mathrm{d}\vec{x} \\ a_{2b}(I^h, J^h) &= \int_{\Omega^h} (\gamma(\vec{x})\beta(\vec{x}) - 1) I^h(\vec{x}) \frac{\partial J^h(\vec{x})}{\partial y} \mathrm{d}\vec{x} \\ a_{2c}(I^h, J^h) &= \int_{\Omega^h} (\gamma(\vec{x})\beta(\vec{x}) - 1) I^h(\vec{x}) \frac{\partial J^h(\vec{x})}{\partial z} \mathrm{d}\vec{x}. \end{aligned}$$

The action of $\mathbb{A}_2$ on a vector $\mathbb{X}$ of order $N_d \cdot n$ may be computed as: $\forall (k,i) \in [\![1; N_d]\!] \times [\![1; n]\!]$,

$$(\mathbb{A}_2 \mathbb{X})_{k+N_d \cdot (i-1)} = \Big(\big(\vec{s}_{k,1} \mathcal{A}_{2a} + \vec{s}_{k,2} \mathcal{A}_{2b} + \vec{s}_{k,3} \mathcal{A}_{2c}\big) [x_{k,1} \cdots x_{k,n}]^T \Big)_i ,$$

where $\vec{s}_{k,j}$ is the jth coordinate of the discrete direction $\vec{s}_k$, for $j \in [\![1; 3]\!]$. Another part of the bilinear form is:

$$a_3(\mathbb{I}^h, \mathbb{J}^h) = \int_{\Omega^h} \gamma(\vec{x}) \big(\mathbb{S} \odot \nabla \mathbb{I}^h(\vec{x})\big) \otimes \big(\mathbb{S} \odot \nabla \mathbb{J}^h(\vec{x})\big) \mathrm{d}\vec{x},$$

assembled as $\mathbb{A}_3$. It is instead possible to assemble the operators $\mathcal{A}_{3a}, \mathcal{A}_{3b}, \mathcal{A}_{3c}, \mathcal{A}_{3d}, \mathcal{A}_{3e}$, and $\mathcal{A}_{3f}$, corresponding to the discretization of the following bilinear forms:

$$\begin{aligned} a_{3a}(I^h, J^h) &= \int_{\Omega^h} \gamma(\vec{x}) \frac{\partial I^h(\vec{x})}{\partial x} \frac{\partial J^h(\vec{x})}{\partial x} \mathrm{d}\vec{x} \\ a_{3b}(I^h, J^h) &= \int_{\Omega^h} \gamma(\vec{x}) \frac{\partial I^h(\vec{x})}{\partial y} \frac{\partial J^h(\vec{x})}{\partial y} \mathrm{d}\vec{x} \\ a_{3c}(I^h, J^h) &= \int_{\Omega^h} \gamma(\vec{x}) \frac{\partial I^h(\vec{x})}{\partial z} \frac{\partial J^h(\vec{x})}{\partial z} \mathrm{d}\vec{x} \\ a_{3d}(I^h, J^h) &= \int_{\Omega^h} \gamma(\vec{x}) \left(\frac{\partial I^h(\vec{x})}{\partial x} \frac{\partial J^h(\vec{x})}{\partial y} + \frac{\partial I^h}{\partial y} \frac{\partial J^h}{\partial x} \right) \mathrm{d}\vec{x} \\ a_{3e}(I^h, J^h) &= \int_{\Omega^h} \gamma(\vec{x}) \left(\frac{\partial I^h(\vec{x})}{\partial x} \frac{\partial J^h(\vec{x})}{\partial z} + \frac{\partial I^h}{\partial z} \frac{\partial J^h}{\partial x} \right) \mathrm{d}\vec{x} \\ a_{3f}(I^h, J^h) &= \int_{\Omega^h} \gamma(\vec{x}) \left(\frac{\partial I^h(\vec{x})}{\partial y} \frac{\partial J^h(\vec{x})}{\partial z} + \frac{\partial I^h}{\partial z} \frac{\partial J^h}{\partial y} \right) \mathrm{d}\vec{x}. \end{aligned}$$

The action of $\mathbb{A}_3$ on a vector $\mathbb{X}$ of order $N_d \cdot n$ may be computed as: $\forall (k,i) \in [\![1; N_d]\!] \times [\![1; n]\!]$,

$$(\mathbb{A}_3 \mathbb{X})_{k+N_d \cdot (i-1)} = \Big(\big(\vec{s}_{k,1}^2 \mathcal{A}_{3a} + \vec{s}_{k,2}^2 \mathcal{A}_{3b} + \vec{s}_{k,3}^2 \mathcal{A}_{3c} + \vec{s}_{k,1} \vec{s}_{k,2} \mathcal{A}_{3d} + \vec{s}_{k,1} \vec{s}_{k,3} \mathcal{A}_{3e} \quad + \vec{s}_{k,2} \vec{s}_{k,3} \mathcal{A}_{3f}\big) [x_{k,1} \cdots x_{k,n}]^T \Big)_i .$$

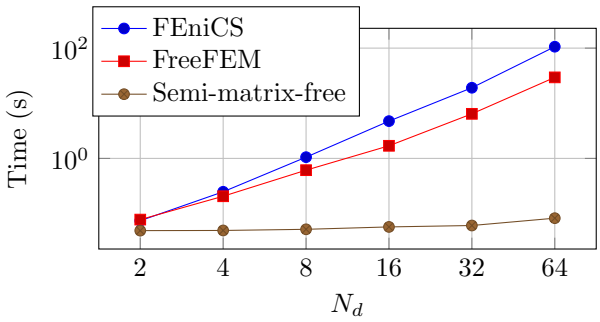

Figure 2: time spent assembling $\mathbb{A}$ from eq. (7) for a two-dimensional domain with $\mathbb{P}_1$ finite elements either explicitly or using our semi-matrix-free approach.

Eventually, the last part of eq. (6) with a volume integral assembled as $\mathbb{A}_4$ to deal with is:

$$a_4(\mathbb{I}^h, \mathbb{J}^h) = \int_{\Omega^h} (\sigma(\vec{x})\Phi \diamond \mathbb{I}^h(\vec{x})) \otimes (\mathbb{J}^h(\vec{x}) + \gamma(\vec{x})\mathbb{S} \odot \nabla \mathbb{J}^h(\vec{x}))\mathrm{d}\vec{x},$$

for which we instead assemble the operators $\mathcal{A}_{4a}, \mathcal{A}_{4b}, \mathcal{A}_{4c}$, and $\mathcal{A}_{4d}$, corresponding to the discretization of the following bilinear forms:

$$\begin{aligned}
a_{4a}(I^h, J^h) &= \int_{\Omega^h} \sigma(\vec{x}) I^h(\vec{x}) J^h(\vec{x})\mathrm{d}\vec{x} \\
a_{4b}(I^h, J^h) &= \int_{\Omega^h} \sigma(\vec{x})\gamma(\vec{x}) I^h(\vec{x}) \frac{\partial J^h(\vec{x})}{\partial x}\mathrm{d}\vec{x} \\
a_{4c}(I^h, J^h) &= \int_{\Omega^h} \sigma(\vec{x})\gamma(\vec{x}) I^h(\vec{x}) \frac{\partial J^h(\vec{x})}{\partial y}\mathrm{d}\vec{x} \\
a_{4d}(I^h, J^h) &= \int_{\Omega^h} \sigma(\vec{x})\gamma(\vec{x}) I^h(\vec{x}) \frac{\partial J^h(\vec{x})}{\partial z}\mathrm{d}\vec{x}.
\end{aligned}$$

Now, one can formally view the column vector $\mathbb{X}$ of dimension $N_d \cdot n$ as a column-major matrix X of dimensions $N_d \times n$. Let $Y = \Phi X$ be of dimensions $N_d \times n$ as well. The action of $\mathbb{A}_4$ on a vector $\mathbb{X}$ of order $N_d \cdot n$ may be computed as:

$$\forall (k,i) \in [\![1; N_d]\!] \times [\![1; n]\!], (\mathbb{A}_4\mathbb{X})_{k+N_d\cdot(i-1)} = \left(\left(\vec{s}_{k,1}\mathcal{A}_{4b} + \vec{s}_{k,2}\mathcal{A}_{4c} + \vec{s}_{k,3}\mathcal{A}_{4d} + \mathcal{A}_{4a}\right)[Y_{k,1} \cdots Y_{k,n}]^T\right)_i.$$

Additional work is needed to take into account the surface integral from eq. (6). It cannot be easily decomposed, neither with FreeFEM nor with FEniCS, in a tensor form, like for the other parts of the variational formulation, because of the Boolean expression in the definition of Γ^- in eq. (2). Thus, for the last line of eq. (6), the operators $\{\mathcal{S}_k\}_{k=1}^{N_d}$ associated with the following bilinear forms have to be evaluated:

$$\forall k \in [\![1; N_d]\!], \zeta_k(I^h, J^h) = \int_{\partial\Omega^h \setminus \Gamma^-} \vec{s}_k \cdot \vec{n}\ I_k^h(\vec{x}) J_k^h(\vec{x})\mathrm{d}\vec{x}. \tag{10}$$

Once again, this would require a number of finite element assemblies that grows linearly with N_d. Hence, it is not tractable for large number of directions. To keep a low number of finite element assemblies, we color the N_{be} boundary elements of $\partial\Omega^h \setminus \Gamma^-$ into subsets $\{\mathcal{F}_k\}_{k=1}^{\chi}$ such that two boundary elements, i.e., faces in 3D or edges in 2D, of $\mathcal{F}_k$, $\forall k \in [\![1; \chi]\!]$, do not share a single vertex. This coloring is computed using a simple greedy algorithm. The following bilinear forms are then assembled into matrices $\{\mathcal{S}'_k\}_{k=1}^{\chi}$:

$$\forall k \in [\![1; \chi]\!], \zeta'_k(I^h, J^h) = \int_{\mathcal{F}_k} I^h(\vec{x}) J^h(\vec{x})\mathrm{d}\vec{x}. \tag{11}$$

Furthermore, given a direction $k \in [\![1; N_d]\!]$, the integrand $\vec{s}_k \cdot \vec{n}$ is constant per boundary element, so these scalar products can be precomputed and stored in $\psi \in \mathbb{R}^{N_d \times N_{\mathrm{be}}}$. For a spatial degree of freedom $i \in [\![1; n]\!]$, $\pi(i)$ returns the subset of boundary elements to which i is associated. For a boundary element $j \in [\![1; N_{\mathrm{be}}]\!]$, $\pi'(j)$ returns the color of the given face. The assembled operators $\{\mathcal{S}_k\}_{k=1}^{N_d}$ which are the discretized counterparts of eq. (10) are thus computed as follows:

$$\forall (k,i,j) \in [\![1; N_d]\!] \times [\![1; n]\!]^2, {\mathcal{S}_k}_{i,j} = \sum_{k=1}^{N_d} \sum_{m \in \pi(i) \cap \pi(j)} \psi_{k,m} {\mathcal{S}'_{\pi'(m)}}_{i,j}. \tag{12}$$

N_d	gemm (ms)	CSR (ms)	GFLOP_{MF} (/s)	GFLOP_{MR}
80	26	115	2 (12)	8
128	48	125	3 (17)	21
320	184	262	10 (22)	129
512	383	395	21 (26)	330
1,280	1,960	1,000	95 (32)	2,060
2,048	4,579	1,574	222 (36)	5,274
5,120	27,281	4,116	1,250 (39)	32,964

Table 1: single-thread performance of the matrix–vector product with an increasing number of directions, for a fixed spatial domain. $n = 44{,}204$, $m = 6.29 \cdot 10^5$, and $m_{\mathcal{S}} = 89{,}483$.

Keep in mind that the matrices $\{\mathcal{S}'_k\}_{k=1}^{\chi}$ are very sparse since they correspond to the discretization of a surface variational formulation. As a consequence, the matrices $\{\mathcal{S}_k\}_{k=1}^{N_d}$ are also sparse, even though eq. (12) uses dense notations for the row and column indices.

For realistic geometries, it is expected that the number of unknowns associated with degrees of freedom on the surface $\partial\Omega^h \setminus \Gamma^-$ will be lower than those associated with degrees of freedom in the volume Ω^h. The cost of evaluating these surface integrals is thus expected to be much lower than the cost of evaluating the fixed number of reference matrices with volume integrals. Using the same test case as for matrix-ready assemblies in section 3.2, FreeFEM is now used to assemble the reference matrices $\mathcal{A}_1, \mathcal{A}_{2a,2b}, \mathcal{A}_{3a,3b,3c,3d}$, and $\mathcal{A}_{4a,4b,4c}$, as well as $\{\mathcal{S}'_k\}_{k=1}^{\chi}$. Note that for two-dimensional test cases, the matrices $\mathcal{A}_{2c}, \mathcal{A}_{3c,3e,3f}$, and $\mathcal{A}_{4d}$ do not exist (only nine reference matrices). As displayed in fig. 2, the semi-matrix-free approach is clearly faster than matrix-ready assemblies by multiple orders of magnitude. Moreover, the cost of this part of the solver is now only loosely dependent on N_d because of the surface integrals. If the coefficient matrix of order $N_d \cdot n$ from eq. (7) is not needed explicitly, we have derived a way to compute implicitly its action on a vector by assembling only reference matrices of order n.

4. Iterative scheme/preconditioning

In the previous paragraph, it was shown how one may assemble auxiliary matrices of a much lower dimension than the original coefficient matrix from eq. (7), to discretize the RTE using the DOM coupled with the FEM. The resulting system, however, still needs to be solved. This is the focus of this section.

4.1. Matrix–vector products

Because the coefficient matrix from eq. (7) is not known explicitly, it seems natural to use for the solution phase methods that only require the action of the matrix on vectors. Krylov methods [63] which are widely used in conjunction with the FEM seem like good candidates. Because they iterate by computing matrix–vector products, it is of paramount importance to design an efficient routine for our semi-matrix-free approach. To do so, a key observation is that, thanks to the compact support of finite element basis functions, the sparsity pattern of all fourteen reference matrices is the same. Thus, no matter the format used to store these sparse matrices, their pattern may be traversed only once. In the case of FreeFEM (and FEniCS), sparse matrices may be stored using the compressed sparse row (CSR) format, which is also widely used in common linear algebra backends such as PETSc [64]. Hence, if all reference matrices have m nonzero coefficients, we will assume that two arrays $\mathcal{I}$ (of size $n+1$) and $\mathcal{J}$ (of size m) are used to traverse the matrices. We also denote by $\mathcal{A}_\star(i)$ the ith nonzero coefficient of the reference matrix $\star$. The same strategy and notations are used for the matrices associated with eq. (10) ($m_{\mathcal{S}}, \mathcal{I}_{\mathcal{S}}, \mathcal{J}_{\mathcal{S}}$, and $\mathcal{S}_\star(i)$). All the previous operations from section 3.3 may now be implemented as in fig. 3. If $\mathbb{A}$ from eq. (7) would have been explicitly assembled, its action on a vector would require $2 \cdot m \cdot N_d^2$ double-precision floating-point operations. Our semi-matrix-free matrix–vector product performs the following number of FLOP:

$$\underbrace{N_d \cdot n \cdot (N_d - 1)}_{\text{line 2 of fig. 3}} + \underbrace{28 \cdot m \cdot N_d}_{\text{lines 4–11}} + \underbrace{2 \cdot m_{\mathcal{S}} \cdot N_d}_{\text{lines 12–16}}. \tag{13}$$

Its efficiency is assessed in table 1. This time, a cube meshed with 235 thousand tetrahedra is used. The corresponding finite element space has 44 thousand degrees of freedom. It is assumed that the matrices $\mathcal{A}_\star$ and $\mathcal{S}_\star$ have already been assembled. The following results have been averaged over five consecutive runs, performed after cache warming. The time spent in the dense matrix–matrix product (line 2) as well as in the CSR traversal (lines 3–17) are reported in the second and third column respectively, with increasing number of directions N_d, reported in the first column. The number of FLOP performed in our product is reported in the fourth column. The numbers in parentheses are the actual throughputs in GFLOP/s of the matrix–vector product. In the fifth

1: **function** $y = \textsc{MatMultAdd}(x, \Phi, \mathcal{I}, \mathcal{J}, \mathcal{A}_\star, \mathcal{I}_\mathcal{S}, \mathcal{J}_\mathcal{S}, \mathcal{S}_\star, \vec{s})$
2: gemm("N", "N", N_d, n, N_d, 1, Φ, N_d, x, N_d, 0, Y, N_d)
3: **do** $i = 0, n$ ▷ row indices
4: **do** $j = \mathcal{I}(i), \mathcal{I}(i+1)$ ▷ column indices of the volume reference matrix
5: **do** $k = 0, N_d$ ▷ direction indices
6: $b_1 = (\mathcal{A}_{2a}(j) + \vec{s}_{k,1}\mathcal{A}_{3a}(j) + \vec{s}_{k,2}\mathcal{A}_{3d}(j) + \vec{s}_{k,3}\mathcal{A}_{3e}(j))\,\vec{s}_{k,1}$
7: $b_2 = (\mathcal{A}_{2b}(j) + \vec{s}_{k,2}\mathcal{A}_{3b}(j) + \vec{s}_{k,3}\mathcal{A}_{3f}(j))\,\vec{s}_{k,2}$
8: $b_3 = (\mathcal{A}_{2c}(j) + \vec{s}_{k,3}\mathcal{A}_{3c}(j))\,\vec{s}_{k,3}$
9: $y(i \cdot N_d + k) = y(i \cdot N_d + k) + \big(\mathcal{A}_1(j) + b_1 + b_2 + b_3\big)x(\mathcal{J}(j) \cdot N_d + k) + \big(\vec{s}_{k,1}\mathcal{A}_{4b}(k) + \vec{s}_{k,2}\mathcal{A}_{4c}(k) + \vec{s}_{k,3}\mathcal{A}_{4d}(k) + \mathcal{A}_{4a}(k)\big)Y(\mathcal{J}(j) \cdot N_d + k)$
10: **end do**
11: **end do**
12: **do** $j = \mathcal{I}_\mathcal{S}(i), \mathcal{I}_\mathcal{S}(i+1)$ ▷ column indices of the surface reference matrix
13: **do** $k = 0, N_d$ ▷ direction indices
14: $y(i \cdot N_d + k) = y(i \cdot N_d + k) + \mathcal{S}_k(j)x(\mathcal{J}_\mathcal{S}(j) \cdot N_d + k)$
15: **end do**
16: **end do**
17: **end do**
18: **end function** ▷ return $y = y + \mathbb{A}x$

Figure 3: matrix–vector product using the semi-matrix-free discretization.

column, knowing that the number of nonzero entries m in each reference matrix is $6.29 \cdot 10^5$, the number of double-precision floating-point operations that would have required a matrix-ready matrix–vector product is reported. For small number of directions ($N_d \leqslant 320$), the performance of our algorithm is constrained by the single traversal of the sparsity pattern of the reference matrices, lines 3–17. With the CSR format, this is known to be an inefficient operation for discretizations on unstructured meshes [65]. When the number of directions becomes greater, the performance is driven by the one of the matrix–matrix product, line 2. Moreover, the vectorization of the inner loops lines 5 and 13 is most efficient for large values of N_d. In general, one may notice that our approach is one order of magnitude more efficient, needing fewer operations, for a wide range of directions. Note that for the case with $N_d = 5{,}120$, if $\mathbb{A}$ were to be assembled explicitly using double-precision floating-point numbers, it would require $6.29 \cdot 10^5 \cdot 5{,}120^2 \cdot 8 \approx 132$ TB of memory (not accounting for integers used to represent the sparsity pattern of $\mathbb{A}$). With the semi-matrix-free approach, this operator is assembled on an ordinary desktop computer. Though the Intel MKL (with AVX-512) is used to perform the matrix–matrix product, we are focused here once again on the single-thread performance of our algorithm on an Intel Xeon Platinum 8168.

4.2. Semi-matrix-free preconditioning

Krylov methods usually require a preconditioner so that they converge in a timely manner to an accurate solution. Because the coefficient matrix from eq. (7) is not assembled explicitly, standard preconditioners such as the restricted additive Schwarz method [66], or algebraic multigrid methods [67], are not usable. Matrix-free solvers typically rely on either: a) basic preconditioners such as the Jacobi method, or b) more sophisticated tools like geometric multigrid methods [68] or element-wise preconditioning [69]. In the case of the RTE, the former certainly makes a Krylov method such as the GMRES [70] converge, but with an insufficient convergence rate. When using different high-level languages, the latter is not easily interoperable since it requires a tight link with the language data structures, e.g., hierarchical meshes. In the next paragraph, an auxiliary operator will be explicitly assembled so that it can be used to precondition eq. (7) using standard techniques.

The diffusion synthetic acceleration (DSA) is a common tool in the radiative transfer community [71, 72] to improve the convergence of iterative schemes when dealing with scattering media with large optical depths. It is based on a simplification of eq. (1) using the diffusion approximation. To build an efficient preconditioner, we use another approximation by assuming that the phase function matrix ϕ in eq. (3) is now diagonal:

$$\forall k \in [\![1; N_d]\!], (\vec{s}_k \cdot \nabla + \beta(\vec{x}))I_k(\vec{x}) = \sigma(\vec{x})\omega_k I_k(\vec{x})\phi_{k,k}.$$

The following physical phenomena are encompassed in these pruned PDEs: transport $\vec{s}_k \cdot \nabla I_k(\vec{x})$, absorption $\kappa(\vec{x})I_k(\vec{x})$, out-scattering $\sigma(\vec{x})I_k(\vec{x})$, and unidirectional in-scattering $\sigma(\vec{x})\omega_k I_k(\vec{x})\phi_{k,k}$. This construction makes the preconditioner able to handle a wide range of radiative transfer problems with absorbing, scattering, transparent, or semi-transparent media, as displayed in the following numerical experiments.

Assembling explicitly the pruned coefficient matrix B from the approximated RTE becomes much cheaper than assembling $\mathbb{A}$, since the dense $N_d \times N_d$ blocks now become diagonal $N_d \times N_d$ blocks. Indeed, the various

function $M = \text{PRUNEDPC}(x, \Phi, \mathcal{I}, \mathcal{J}, \mathcal{A}_\star, \vec{s})$
  allocate $\mathcal{I}_B$ to store $N_d \cdot n + 1$ integers
  allocate $\mathcal{J}_B$ to store $N_d \cdot m$ integers
  allocate $\mathcal{B}$ to store $N_d \cdot m$ scalars
  do $i = 0, n$ ▷ row indices
    $m_{\text{row}} = \mathcal{I}(i+1) - \mathcal{I}(i)$; $j_{\text{shifted}} = N_d \cdot \mathcal{I}(i)$
    do $k = 0, N_d$ ▷ direction indices
      $\mathcal{I}_B(N_d \cdot i + k) = j_{\text{shifted}} + k \cdot m_{\text{row}}$ ▷ number of nonzeros of this row
      do $j = \mathcal{I}(i), \mathcal{I}(i+1)$ ▷ column indices of the volume reference matrix
        $\text{idx} = j_{\text{shifted}} + k \cdot m_{\text{row}} + (j - \mathcal{I}(i))$
        $\mathcal{J}_B(\text{idx}) = \mathcal{J}(j) \cdot N_d + k$ ▷ column index of the pruned preconditioner
        $b_1 = (\mathcal{A}_{2a}(j) + \vec{s}_{k,1}\mathcal{A}_{3a}(j) + \vec{s}_{k,2}\mathcal{A}_{3d}(j) + \vec{s}_{k,3}\mathcal{A}_{3e}(j))\,\vec{s}_{k,1}$
        $b_2 = (\mathcal{A}_{2b}(j) + \vec{s}_{k,2}\mathcal{A}_{3b}(j) + \vec{s}_{k,3}\mathcal{A}_{3f}(j))\,\vec{s}_{k,2}$
        $b_3 = (\mathcal{A}_{2c}(j) + \vec{s}_{k,3}\mathcal{A}_{3c}(j))\,\vec{s}_{k,3}$
        $\mathcal{B}(\text{idx}) = \mathcal{B}(\text{idx}) + \mathcal{A}_1(j) + b_1 + b_2 + b_3 + \left(\vec{s}_{k,1}\mathcal{A}_{4b}(k) + \vec{s}_{k,2}\mathcal{A}_{4c}(k) + \vec{s}_{k,3}\mathcal{A}_{3d}(k) + \mathcal{A}_{4a}(k)\right)\Phi_{k,k}$
      end do
    end do
  end do
  $\mathcal{I}_B(N_d \cdot n) = N_d \cdot m$ ▷ total number of nonzeros
end function ▷ return $B = \text{CSR}(\mathcal{I}_B, \mathcal{J}_B, \mathcal{B})$

Figure 4: explicit assembly of the pruned preconditioner.

N_d	Assembly (s)	n_B	m_B	Setup (s)
80	1.9	$4 \cdot 10^6$	$5 \cdot 10^7$	9.1
128	2.9	$6 \cdot 10^6$	$8 \cdot 10^7$	15.4
320	7.5	$1 \cdot 10^7$	$2 \cdot 10^8$	42.5
512	12.1	$2 \cdot 10^7$	$3 \cdot 10^8$	72.7
1,280	31.0	$6 \cdot 10^7$	$8 \cdot 10^8$	198.2
2,048	53.0	$9 \cdot 10^7$	$1 \cdot 10^9$	317.5
5,120	102.1	$2 \cdot 10^8$	$3 \cdot 10^9$	1,181.7

Table 2: time spent assembling the pruned preconditioner. n_B and m_B represent the order and the number of nonzero entries respectively in B.

components of $\mathbb{I}^h$ in eq. (6) are only coupled through Φ. The assembly cost is thus divided by N_d. Zero off-diagonal coefficients from the dense blocks of B are obviously not stored. Thus, there is no block structure in B and it is assumed that it is stored in a standard sparse matrix using the CSR format. Its arrays are noted $\mathcal{I}_B, \mathcal{J}_B$, and $\mathcal{B}$. In fig. 4, the procedure used to allocate and assemble the pruned preconditioner is displayed. For the same test case as in table 1 and on the same hardware, the time spent in this routine is shown in the second column of table 2, averaged over two runs. In the third (resp. fourth) column, the order of the system (resp. number of nonzero entries) is displayed. Choosing an efficient preconditioner to approximate the action of B^{-1} is not trivial. In our experiments, we used *hypre* algebraic multigrid solver BoomerAMG [73] with the following parameters: ext+i interpolation, HMIS coarsening, two sweeps of l_1 Gauss–Seidel smoothing per level, and aggressive coarsening on all levels. Similar parameters are used in the neutron transport community [74]. In the fifth column of table 2, the time spent in BoomerAMG for constructing the preconditioner is reported. Obviously, with a fixed spatial mesh but a refined angular mesh, a steady increase in setup time is observed. In the following section, a strategy to mitigate this issue will be presented, based on a hybrid multigrid in space–domain decomposition in angles preconditioner.

5. Large-scale numerical results

Both the matrix–vector product and the preconditioner have been defined in the previous paragraphs. In this section, the performance of the complete solver will be assessed for large-scale simulations. One application of the solver is its use to improve the design of heterogeneous participating media for material science. Thus, for a given geometry, multiple problems have to be solved, for example because of changing physical properties. In [75], this solver is used to study the response of open-cell foams made of SiC or Al_2O_3 to radiations, which represent two different classes of materials (opaque or semi-transparent). We will thus focus on the strong scaling of the solver. However, since the transport community is heavily focused on weak scaling, there is also

such an analysis in section 6.4. Before presenting any scaling tests of the solver, it is first validated in the next paragraph.

5.1. Validation

Problems 3i and 3ii from Kobayashi benchmarks [76] are used to validate the solver. These test cases correspond to monochromatic emitting source radiation problems within heterogeneous materials with purely reflecting walls. They have already been used to validate radiation transport solvers in the literature [77, 78, 79].

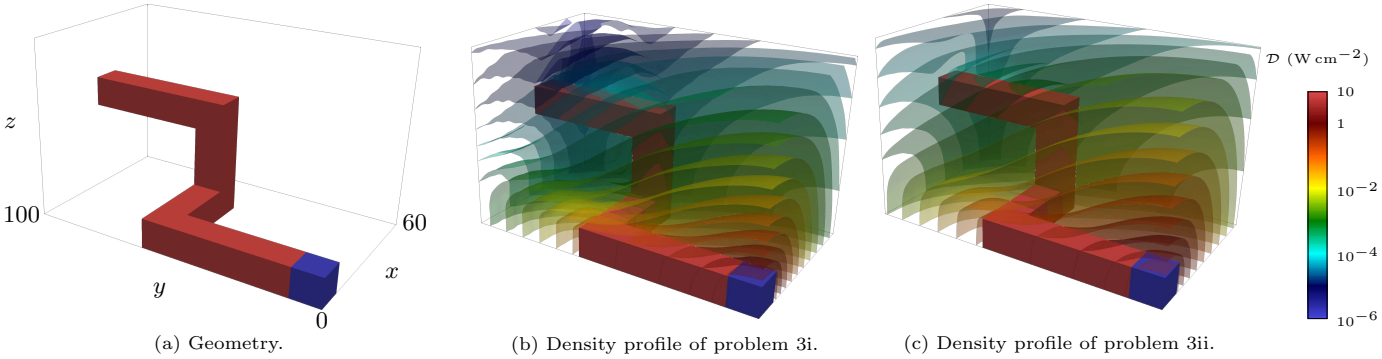

(a) Geometry. (b) Density profile of problem 3i. (c) Density profile of problem 3ii.

Figure 5: Kobayashi benchmark.

The material geometry for both problems 3i and 3ii is a $60 \times 100 \times 60\,\mathrm{cm}^3$ rectangular cuboid which consists of three regions: source, void, and shield. They are respectively highlighted in blue, red, and transparent in fig. 5a. The radiative exchange in both of these problems is driven by the source region, a $10 \times 10 \times 10\,\mathrm{cm}^3$ cube located at the origin of the coordinate system. It emits a black-body radiation of unit strength. The xz-plane for $y = 0$, xy-plane for $z = 0$, and yz-plane for $x = 0$, i.e., front, bottom, and left planes, are specularly reflecting, while the three other planes are vacuum walls. Problem 3i involves absorption, emission, and reflection but neglects scattering. The coefficients (κ, σ) are constant per region: $(0.1\,\mathrm{cm}^{-1}, 0\,\mathrm{cm}^{-1})$ in the source, $(10^{-4}\,\mathrm{cm}^{-1}, 0\,\mathrm{cm}^{-1})$ in the void, and $(0.1\,\mathrm{cm}^{-1}, 0\,\mathrm{cm}^{-1})$ in the shield region. Problem 3ii involves all modes of radiation: absorption, emission, scattering, and reflection. The coefficients are now: $(0.05\,\mathrm{cm}^{-1}, 0.05\,\mathrm{cm}^{-1})$, $(5 \cdot 10^{-5}\,\mathrm{cm}^{-1}, 5 \cdot 10^{-5}\,\mathrm{cm}^{-1})$, and $(0.05\,\mathrm{cm}^{-1}, 0.05\,\mathrm{cm}^{-1})$, respectively.

Problems 3i and 3ii are prone to ray effects and not trivial to solve with the DOM [78]. As such, these benchmarks require a fine spatial and angular meshes, cf. fig. 1. This mitigates errors due to ray effects. Two sets of meshes were used with our solver to further quantify ray effects and validate our results. A coarse set made of a spatial mesh with $1.41 \cdot 10^5$ nodes and $8.15 \cdot 10^5$ elements and an angular mesh with 320 directions. And a fine set made of a spatial mesh with $7.88 \cdot 10^5$ nodes and $4.71 \cdot 10^6$ elements and an angular mesh with 5,120 directions. As suggested in Kobayashi benchmark document [76], densities are extracted at certain point locations within the materials. Table 3 provides these specific densities obtained with four different approaches:

1. numerical evaluation of an exact expression only available for problem 3i [76], column "reference",
2. Monte Carlo solver [80], column "MC",
3. spherical harmonics P_{21} solver [77], column "P_{21}",
4. our solver with both sets of meshes, column "$\mathrm{DOM_c}$" and "$\mathrm{DOM_f}$" for the coarse and the fine set, respectively.

The data provided in the table suggests that the density computed by our solver when using the fine set of meshes are in close agreement with the ones provided by other approaches. Moreover for both problems 3i and 3ii, the accuracy of the results improves significantly when switching from the coarse to the fine set of meshes. Contours of the density in logscale are presented in fig. 5b (resp. fig. 5c) for problem 3i (resp. 3ii).

5.2. Parallelism

Workload distribution. The finite element method is most often parallelized on distributed-memory systems using a coarse-grained approach such as domain decomposition. One of the many linear algebra backends that does support this workload distribution is PETSc, that will be used in all the following tests. Considering that an input mesh is split into P domains using a mesh partitioner such as Metis [81], FreeFEM is in charge of generating a global unknown numbering of $\mathcal{V}^h$. This numbering is such that all P processes will own a contiguous chunk of rows of all reference matrices $\mathcal{A}_\star$ (one-dimensional row-wise distribution).

Table 3: density ($\mathrm{W\,cm^{-2}}$) of Kobayashi problems 3i and 3ii computed with: an exact expression [76], GMVP [80], Ardra [77] or our solver, for $x = z = 5\,\mathrm{cm}$.

	Problem 3i					Problem 3ii			
y	Reference	MC	P_{21}	$\mathrm{DOM_c}$	$\mathrm{DOM_f}$	MC	P_{21}	$\mathrm{DOM_c}$	$\mathrm{DOM_f}$
5	$5.96 \cdot 10^{0}$	$5.94 \cdot 10^{0}$	$5.96 \cdot 10^{0}$	$6.1 \cdot 10^{0}$	$5.96 \cdot 10^{0}$	$8.62 \cdot 10^{0}$	$8.61 \cdot 10^{0}$	$8.8 \cdot 10^{0}$	$8.63 \cdot 10^{0}$
15	$1.37 \cdot 10^{0}$	$1.37 \cdot 10^{0}$	$1.34 \cdot 10^{0}$	$1.4 \cdot 10^{0}$	$1.37 \cdot 10^{0}$	$2.16 \cdot 10^{0}$	$2.13 \cdot 10^{0}$	$2.2 \cdot 10^{0}$	$2.16 \cdot 10^{0}$
25	$5.01 \cdot 10^{-1}$	$5.01 \cdot 10^{-1}$	$4.95 \cdot 10^{-1}$	$5.1 \cdot 10^{-1}$	$5.00 \cdot 10^{-1}$	$8.94 \cdot 10^{-1}$	$8.84 \cdot 10^{-1}$	$9.0 \cdot 10^{-1}$	$8.93 \cdot 10^{-1}$
35	$2.52 \cdot 10^{-1}$	$2.53 \cdot 10^{-1}$	$2.49 \cdot 10^{-1}$	$2.6 \cdot 10^{-1}$	$2.50 \cdot 10^{-1}$	$4.78 \cdot 10^{-1}$	$4.72 \cdot 10^{-1}$	$4.8 \cdot 10^{-1}$	$4.74 \cdot 10^{-1}$
45	$1.50 \cdot 10^{-1}$	$1.50 \cdot 10^{-1}$	$1.56 \cdot 10^{-1}$	$1.4 \cdot 10^{-1}$	$1.48 \cdot 10^{-1}$	$2.89 \cdot 10^{-1}$	$2.99 \cdot 10^{-1}$	$2.8 \cdot 10^{-1}$	$2.87 \cdot 10^{-1}$
55	$9.92 \cdot 10^{-2}$	$9.92 \cdot 10^{-2}$	$1.20 \cdot 10^{-1}$	$8.3 \cdot 10^{-2}$	$9.84 \cdot 10^{-2}$	$1.93 \cdot 10^{-1}$	$2.24 \cdot 10^{-1}$	$1.7 \cdot 10^{-1}$	$1.91 \cdot 10^{-1}$
65	$4.23 \cdot 10^{-2}$	$4.23 \cdot 10^{-2}$	$5.10 \cdot 10^{-2}$	$3.9 \cdot 10^{-2}$	$4.20 \cdot 10^{-2}$	$1.05 \cdot 10^{-1}$	$1.19 \cdot 10^{-1}$	$9.9 \cdot 10^{-2}$	$1.04 \cdot 10^{-1}$
75	$1.15 \cdot 10^{-2}$	$1.15 \cdot 10^{-2}$	$8.91 \cdot 10^{-3}$	$1.2 \cdot 10^{-2}$	$1.14 \cdot 10^{-2}$	$3.38 \cdot 10^{-2}$	$3.02 \cdot 10^{-2}$	$3.4 \cdot 10^{-2}$	$3.35 \cdot 10^{-2}$
85	$3.25 \cdot 10^{-3}$	$3.25 \cdot 10^{-3}$	$1.95 \cdot 10^{-3}$	$3.4 \cdot 10^{-3}$	$3.33 \cdot 10^{-3}$	$1.08 \cdot 10^{-2}$	$8.54 \cdot 10^{-3}$	$1.1 \cdot 10^{-2}$	$1.08 \cdot 10^{-2}$
95	$9.48 \cdot 10^{-4}$	$9.49 \cdot 10^{-4}$	$6.82 \cdot 10^{-4}$	$7.7 \cdot 10^{-4}$	$9.69 \cdot 10^{-4}$	$3.40 \cdot 10^{-3}$	$2.83 \cdot 10^{-3}$	$3.0 \cdot 10^{-3}$	$3.40 \cdot 10^{-3}$

Matrix–vector product. As it is the case with standard matrix types from PETSc (and other backends like *hypre* [82]), it is furthermore assumed that the local representation of each matrix $\mathcal{A}_\star$ is split into two matrices $\{D_i\}_{i=1}^{P}$ and $\{O_i\}_{i=1}^{P}$, where the unknowns associated with the $\{D_i\}_{i=1}^{P}$ are purely local to each domain, whereas those associated with the $\{O_i\}_{i=1}^{P}$ involve interprocess communication for computing matrix–vector products, cf. [83]. By using a matrix of type "shell", one can wrap the matrix–vector product from fig. 3 so that PETSc will use it in its Krylov solvers. If the reference matrices are split using the previous decomposition, it is trivial to extend the algorithm so that it overlaps communication due to interprocess unknowns shared with neighboring domains with local computation.

Pruned preconditioner. In the previous paragraphs, matrix-free system eq. (7) is solved by using an assembled preconditioner B defined in section 4.2. The strategy used to assemble B was to prune all off-diagonal nonzeros in the $N_d \times N_d$ dense blocks of $\mathbb{A}$. The pruned operator B of dimension $N_d \cdot n$ thus still remains structured, with blocks of dimension N_d, but they are now diagonal instead of dense. As displayed in the previous section in table 2, setting up BoomerAMG on the complete pruned operator B becomes costly for large numbers of directions. To decrease the setup cost, we propose to modify the preconditioner by first using a domain decomposition-like approach in angles, and then using multigrid in space. Instead of using a single instance of BoomerAMG with the single operator B, each structured diagonal block of dimension N_d will be decomposed into q subblocks, where q is a common divisor of the number of directions N_d and the number of processing elements P. This may be interpreted as nonoverlapping domain decomposition according to the angles. Then, q instances of BoomerAMG are created for each subsystem of dimension $\frac{N_d}{q} \cdot n$. This is standard multigrid in space. Suitable restriction and interpolation operators will be defined later on to go from the full space to a single subsystem and vice versa. This is somehow similar to the anglesets strategy from [40]. From an algebraic point of view, the modified pruned preconditioner is now written as:

$$B^{-1} = \sum_{k=1}^{q} R_k^T (R_k B R_k^T)^{-1} R_k,$$

where q is a common divisor of the number of directions N_d and the number of processing elements P, and R_k is the restriction on the kth angleset. Formally, for each spatial unknown, R_k selects from all N_d directions only the $M_q = N_d/q$ ones from the appropriate angleset. In matrix form, R_k is a full-rank diagonal Boolean matrix written as:

$$\forall k \in [\![1; q]\!], R_k = \begin{bmatrix} J_k & & \\ & \ddots & \\ & & J_k \end{bmatrix} \in \{0,1\}^{n \cdot M_q \times n \cdot N_d},$$

with $J_k = \begin{bmatrix} \mathbb{0}_{M_q \times (k-1) \cdot M_q} & \mathbb{1}_{M_q} & \mathbb{0}_{M_q \times (q-k) \cdot M_q} \end{bmatrix} \in \{0,1\}^{M_q \times N_d}$. Within the PETSc framework, this construction of B^{-1} could be performed using an additive fieldsplit preconditioner (with as many fields as anglesets), but this would have two main bottlenecks:

- the operator B would have to be assembled explicitly first,
- q would need to be low for the preconditioner assembly to be efficient.

Instead, as it is standard when doing domain decomposition in space, the respective $\left\{R_k B R_k^T\right\}_{k=1}^{q}$ are directly assembled on q different MPI communicators of size P/q. This can be done by looping on the appropriate directions from a given angleset line 7 from fig. 4, instead of looping on all N_d directions. For better memory efficiency, we use PETSc matrices of type "hypre" to store these operators, so that there is no copy or conversion

from the default PETSc type "aij" to "hypre". Once the problem has been decomposed in angles, q instances of BoomerAMG are called concurrently to approximate the action of each $\left\{(R_k B R_k^T)^{-1}\right\}_{k=1}^{q}$ (multigrid in space), using the same parameters as in section 3.3.

5.3. Test case and scaling

Hardware and software settings. Results were obtained on a partition of Irène composed of 1,656 nodes with two 24-core Intel Skylake clocked at 2.7 GHz. The interconnect is an InfiniBand EDR full fat tree and the MPI implementation exploited was IntelMPI version 2019.0.5.281. All binaries and shared libraries were compiled with Intel compilers and Math Kernel Library support (for dense linear algebra computations) version 19.0.5.281. PETSc version 3.12.4 with *hypre* version 2.18.2 were used.

Geometry and physics. For the spatial domain, a three-dimensional centimetric rectangular cuboid of dimension $[0;1] \times [0;1] \times [0;3]$ is used. In the rectangular cuboid lies a collection of multiple small spheres with varying physical parameters, cf. fig. 6. The resulting mesh generated by Gmsh [84] is made of 1.9 million tetrahedra, which are uniformly refined once, for a total of $8 \times 1.9 = 15$ million tetrahedra. Before the refinement step, the unstructured mesh is partitioned in parallel using ParMETIS [85]. The background coefficients used in the rectangular cuboid are: $\kappa = 10^{-6}\,\mathrm{cm}^{-1}$ and $\sigma = 10^{-6}\,\mathrm{cm}^{-1}$, i.e., a nearly transparent medium. In the spheres, the values of this pair of coefficients vary between: $\left\{\{10^{-6}, 10\}, \{10, 10^{-6}\}, \{0.1, 0.1\}, \{10, 10\}\right\}$. These values represent a mix of highly scattering, highly absorbing, and semi-transparent materials. They are considered homogenized with ϕ modeled using the Henyey–Greenstein phase function [86], with the anisotropy factor $g = 0.5$. As inflow boundary conditions, the rectangular cuboid is impinged with a collimated external radiative source $\mathbb{I}_{\text{inflow}}$ on its left face:

$$\mathbb{I}_{\text{inflow}} = I_0 \mathbb{1}_{(\vec{x},\vec{s}) \in \{0\} \times [0.25;0.75] \times [0.25;0.75] \times \{[1,0,0]^T\}},$$

where $I_0 = 1\,\mathrm{W\,cm^{-2}\,sr^{-1}}$. $\mathbb{1}$ represents the vectorial characteristic function of a set. Since emission is neglected and the condition on angles reads $\vec{s} \in \{[1,0,0]^T\}$, the right-hand side $\mathbb{B}$ of eq. (7) is nonzero for a single component I^h associated with this direction. In total, $N_d = 5{,}120$ directions are used to discretize the unit sphere, cf. fig. 1b. This is an extremely fine angular mesh. Such a resolution will be necessary in a following test when dealing with specular reflections on spheres in order to solve the physics accurately [32]. These directions are grouped in $q = 32$ anglesets of dimension $N_d/q = 160$. To the best of our knowledge, radiative transfer equation solvers using Krylov methods have never been able to deal with such an angular resolution, mostly due to memory limitations. After a simple post-processing step, it is easy to compute the spatial density profile $\mathcal{D}$, i.e., at the continuous level, the integral over the complete solid angle of the radiative intensity, by computing for each spatial degree of freedom: $\forall j \in [\![1;n]\!], \mathcal{D}_j \approx \sum_{i=1}^{N_d} \omega_i x_{i,j}$, assuming x is the solution vector from eq. (7). For this test, the density is shown in fig. 7. Notice the jumps in the density due to the presence of spheres with nonzero extinction coefficients along the collimated radiation.

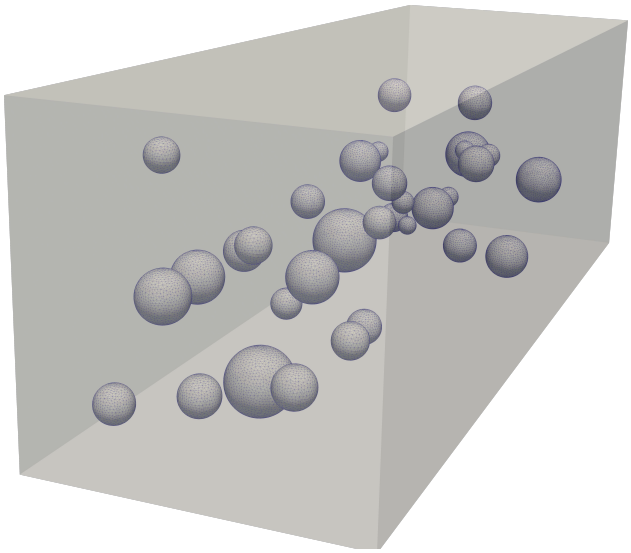

Figure 6: Gmsh geometry for the large-scale experiments.

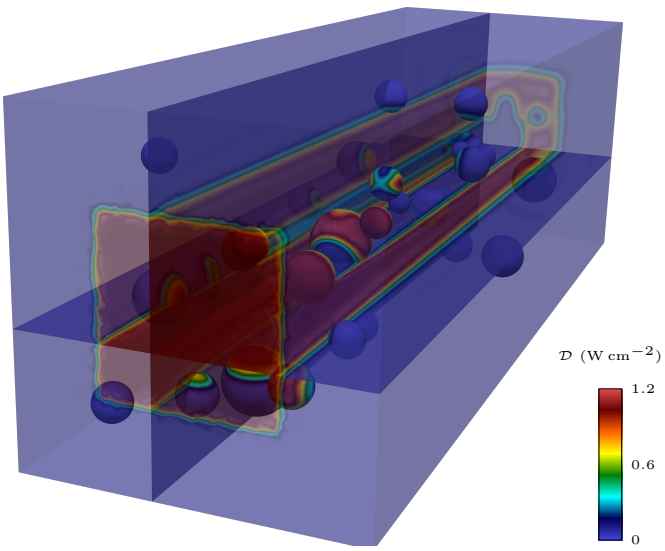

Figure 7: density profile $\mathcal{D}$. The rectangular cuboid is impinged on the front face and the radiation travels up to the back face, while being partially absorbed in the spheres.

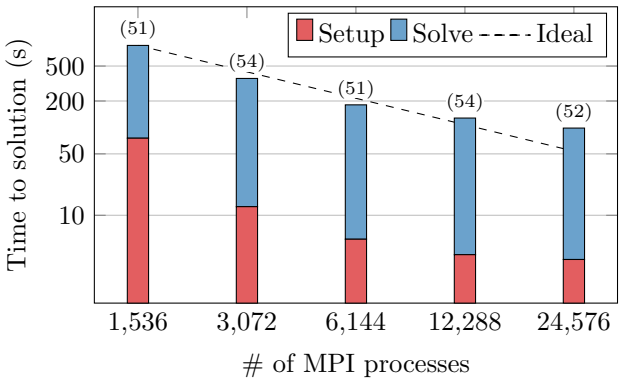

(a) Time to solution. Each color represents the fraction of the total time spent in the respective tasks. In parenthesis, number of iterations.

P	Setup (s)	Solve (s)	# of iterations	Speedup
1,536	549.6	309.1	51	–
3,072	155.1	206.2	54	2.4
6,144	58.3	122.5	51	4.7
12,288	33.5	94.4	54	6.7
24,576	24.5	73.8	52	8.7

(b) Timings of the setup and the solution phases.

Figure 8: strong scaling analysis of the complete solver for a system of thirteen billion unknowns (without reflection).

Performance. In the following numerical experiments and as standard in the radiative transfer community [49, 57, 87], convergence is assumed to be reached when the relative residual norm is lower than 10^{-6}. Such a stopping criterion provided accurate final residuals[1]. Since the global operator is ill-conditioned, the long-recurrence Krylov method GMRES(30)[2] using double-precision floating-point numbers is preferred over short-recurrence methods such as BiCGSTAB, cf. [17] for a comparison with radiative transfer operators.

The performance of the complete solver is assessed in the strong scaling regime on 1,536 up to 24,576 MPI processes in fig. 8. The following steps of our method are timed, and averaged over two consecutive runs (same node distribution): assembly of the reference matrices $\mathcal{A}_\star$ and of the surface integrals (section 3.3), of the preconditioner B (section 4.2), and preconditioner setup (all three steps are summed and referenced to as the "setup" phase), and solution phase. In fig. 8a, each color represents the fraction of the total time spent in these two phases. For example, with 1,536 MPI processes, the height of the red bar is $\frac{549.6}{549.6+309.1} = 64\%$ of the height of the complete bar (figures taken from table 8b). These two colors are used to differentiate at a glance both phases, in order to estimate the setup time to solve time ratio. This may be useful to infer how to amortize setup costs when doing successive linear solves. For the exact timings, interested readers are referred to the right-hand side table. Overall, even with a rather high number of anglesets and aggressive multigrid parameters, the preconditioner remains very robust in terms of iterations on a wide range of MPI process counts. The test case was chosen so that it saturates the node memory when running on 1,536 MPI processes. For moderate number of MPI processes, computations (and thus cache effects) prevail over communications, which explains ideal speedups. At scale, the total time starts to be dominated by the solution phase. Indeed, on 24,576 processes, the average number of tetrahedra per process is a mere 610, so that the communication cost in the matrix–vector product cannot be fully overlapped and is no more negligible compared to the highly efficient computation, cf. table 1. For this largest configuration, the average grid and operator complexities of $\left\{(R_k B R_k^T)^{-1}\right\}_{k=1}^{32}$, as returned by *hypre*, are 1.09 and 1.17 respectively. These low numbers imply that most of the communications take place in the matrix–vector products. Note that their volume of communication is proportional to N_d, while their computational cost is proportional to N_d^2, cf. eq. (13).

6. Specular reflections

In the previous sections, a solver for the radiative transfer equation was derived using a mixed matrix-ready/matrix-free approach. The goal of the following paragraphs is to show how this solver may be extended to deal with specular reflections. Such phenomena appear when radiations reach surfaces with different reflective indices. The radiative intensity is thus modified since a portion of the incident radiations is reflected back into the domain, according to Fresnel equations.

6.1. Assembly

To take into account these reflections, the bilinear form from eq. (6) has to be modified. Indeed, it is now assumed that the inflow boundary condition for all $\{I_k^h\}_{k=1}^{N_d}$ is given, for all $(\vec{x}, \vec{s}_k) \in \Gamma^-$, by:

$$I_k^h = I_{k,\text{inflow}} + \sum_{\substack{j \in [\![1;N_d]\!] \\ \vec{s}_j \cdot \vec{n} > 0}} \rho_{\vec{n},k,j} I_j^h. \tag{14}$$

[1] checked with the PETSc option `-ksp_view_final_residual`

[2] the default restart value of PETSc

Describing precisely how the coefficients ρ are computed is beyond the scope of this paper. There are various ways to do so, for example using the 1-DP (used in this paper), 3-DP, or the partition methods [88]. Their values depend on the reflective index of the surface material, the direction of the normal $\vec{n}$ at the point of reflection, as well as the incident and reflected directions $\vec{s}_k$ and $\vec{s}_j$. It is assumed that the reflective surface Γ^- may be decomposed into a union of surfaces with p different normals, i.e., $\Gamma^- = \cup_{r=1}^{p} \Gamma_r^-$. For example, if Ω^h is a hexahedron, p is equal to six. With the new inflow boundary condition, for all components of $\mathbb{I}^h$, the bilinear form a of eq. (6) has to be augmented by the following surface integral, for each component:

$$a(\mathbb{I}^h, \mathbb{J}^h) \mathrel{+}= \sum_{r=1}^{p} \int_{\Gamma_r^-} (\mathcal{P}_r \diamond \mathbb{I}^h(\vec{x})) \otimes \mathbb{J}^h(\vec{x}) \mathrm{d}\vec{x}, \tag{15}$$

with the matrices $\{\mathcal{P}_r\}_{r=1}^{p}$ being defined as:

$$\forall r \in [\![1; p]\!], \mathcal{P}_r = \begin{bmatrix} \rho_{\vec{n},1,1} & \cdots & \rho_{\vec{n},1,N_d} \\ \vdots & \ddots & \vdots \\ \rho_{\vec{n},N_d,1} & \cdots & \rho_{\vec{n},N_d,N_d} \end{bmatrix}.$$

For all $(\vec{x}, \vec{s}_k) \in \Gamma^-$, $\vec{s}_k \cdot \vec{n} < 0$, cf. the definition of Γ^- given eq. (2). To take into account the conditional sum from eq. (14), $\vec{s}_j \cdot \vec{n} > 0$, the diagonals of $\{\mathcal{P}_r\}_{r=1}^{p}$ are set to zero. Moreover, since a large number of directions are used, these matrices are relatively sparse. In practice, they are stored using the coordinate list format. As in section 3.3, instead of assembling the vectorial bilinear form (15), the following variational formulations are assembled:

$$\forall r \in [\![1; p]\!], q_r(I^h, J^h) = \int_{\Gamma_r^-} I^h(\vec{x}) J^h(\vec{x}) \mathrm{d}\vec{x}.$$

Let n_{Γ^-} (resp. $\{n_{\Gamma_r^-}\}_{r=1}^{p}$) be the number of unknowns from $\mathcal{V}^h$ associated with elements of Γ^- (resp. $\{\Gamma_r^-\}_{r=1}^{p}$). The assembly cost of eq. (15) is proportional to $N_d \cdot n_{\Gamma^-}$, while the total assembly cost of all reference matrices from the previous equation is proportional to $\sum_{r=1}^{p} n_{\Gamma_r^-}$.

6.2. Matrix–vector products

The initial algorithm from fig. 3 has to be extended to take into account the reference matrices from the previous paragraph. It is assumed that the bilinear forms $\{q_r\}_{r=1}^{p}$ are assembled using the CSR format $\{\mathcal{I}_{q_r}, \mathcal{J}_{q_r}, \mathcal{Q}_r\}_{r=1}^{p}$. This time, the sparsity pattern of the reference matrices corresponding to the surface integral may be different. For a surface $r \in [\![1; p]\!]$, and for all unknown indices $i \in [\![1; n_{\Gamma_r^-}]\!]$, we assume that $n_{\Gamma_r^-}(i)$ returns the unknown index in the finite element space $\mathcal{V}^h$. The extended matrix–vector algorithm is presented in fig. 9. For each reflective surface, it involves first gathering the relevant values from the input vector of size $N_d \cdot n$, then computing a sparse matrix–dense matrix product, and eventually, scattering back the result into the output vector. When dealing with meshes with a large amount of different reflective surfaces (large p), this algorithm may not scale well. However, it is important to keep in mind that for realistic three-dimensional geometries, the number of unknowns associated with surface elements n_{Γ^-} is expected to be much lower than the global number of unknowns n. Thus, the most time-consuming part of the matrix–vector procedure should still be the algorithm from fig. 3.

Because of the definition of $\{\mathcal{P}_r\}_{r=1}^{p}$, eq. (15) would not introduce any diagonal values in the dense $N_d \times N_d$ blocks of $\mathbb{A}$ from eq. (7) if it were to be assembled explicitly. Thus, the definition of the preconditioning matrix B from section 4.2 will remain the same for the numerical experiments.

6.3. Test case and scaling

The same geometry with the same background coefficients from section 5.3 will be used. The main difference now is that all the spheres inside the rectangular cuboid model reflecting materials with no transmissivity. As such, their insides are not meshed anymore, and their reflective indices are picked from the following set: {1.8, 2.0, 2.2, 2.5}. The number of directions is still set to $N_d = 5{,}120$, and with a mesh of 14.5 million tetrahedra, the discrete system is of order 14×10^9. The outer surface of the rectangular cuboid is nonreflective (reflective index set to one). The same preconditioner as before is used: hybrid multigrid in space–domain decomposition in angles with the same BoomerAMG parameters and $q = 32$ anglesets. In the density now displayed in fig. 10, one can see that at the surface of the spheres in the rectangular cuboid, part of the radiative intensity is reflected back into the spatial domain. The impact of reflections that cause more variations in the density profile compared to fig. 7 may also be observed. Notice that for this test case, the total number of reflective surfaces p is equal to 407. Depending on how the global domain is decomposed, each process has a different number of local reflective surfaces $\{p_i\}_{i=1}^{P}$. Accordingly, they only load the corresponding matrices $\{\mathcal{P}_r\}_{r=1}^{p_i}$ that are generated in a pre-processing step. As these numbers decrease, so does the local cost of the matrix–vector product (outer loop line 2 from fig. 9). For this configuration, the performance of the solver, cf. fig. 11, delivers similar speedups as in the previous section (without reflective surface).

```
1: function y = MatMultAdd(x, {P_r, I_{q_r}, J_{q_r}, Q_r}_{r=1}^p)
2:   do r = 1, p
3:     allocate Y to store N_d · n_{Γ_r^-} scalars
4:     allocate tmp to store N_d · n_{Γ_r^-} scalars
5:     do i = 0, n_{Γ_r^-}
6:       do k = 0, N_d
7:         Y(N_d · i + k) = x(N_d · n_{Γ_r^-}(i) + k)
8:       end do
9:     end do
10:    tmp = P_r Y
11:    do i = 0, n_{Γ_r^-}
12:      do j = I_{q_r}(i), I_{q_r}(i + 1)
13:        do k = 0, N_d
14:          idx = N_d · n_{Γ_r^-}(i) + k
15:          y(idx) = y(idx) + tmp(N_d · i + k) Q_r(j)
16:        end do
17:      end do
18:    end do
19:  end do
20: end function
```

Figure 9: matrix–vector product for taking reflections into account.

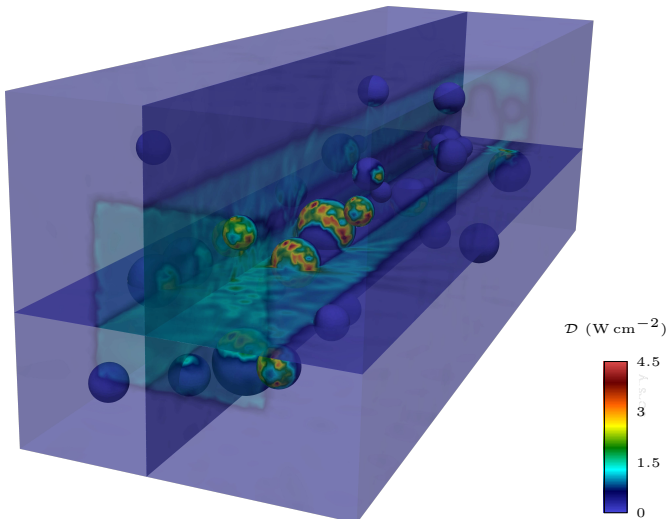

Figure 10: density profile $\mathcal{D}$ when dealing with reflective surfaces. The rectangular cuboid is impinged on the front face and the radiation travels up to the back face, while being reflected on the surface of the spheres.

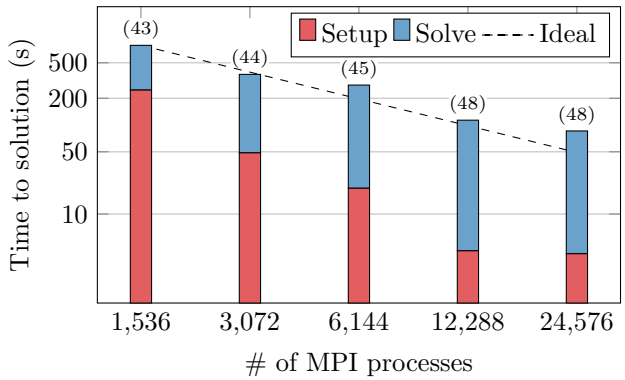

(a) Time to solution. Each color represents the fraction of the total time spent in the respective tasks. In parenthesis, number of iterations.

P	Setup (s)	Solve (s)	# of iterations	$\max\{p_i\}_{i=1}^P$
1,536	649.5	136.4	43	156
3,072	243.6	127.3	44	89
6,144	148.1	133.1	45	79
12,288	32.4	81.0	48	53
24,576	24.6	61.2	48	37

(b) Timings of the setup and the solution phases. The last column provides the maximum number of local reflective surfaces (which depends on the domain decomposition).

Figure 11: strong scaling analysis of the complete solver for a system of fourteen billion unknowns (with reflections).

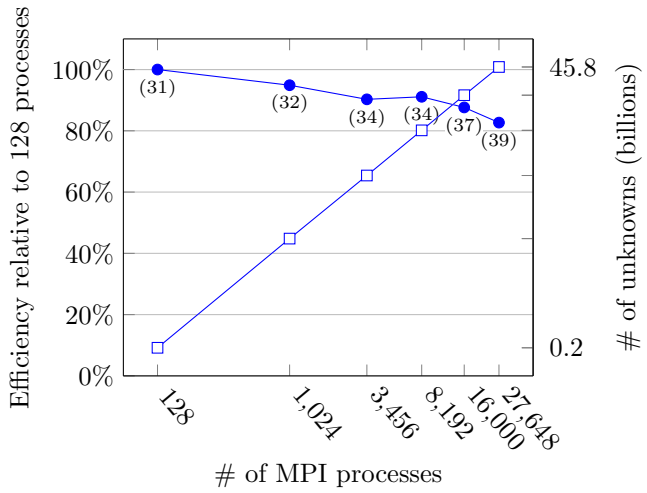

(a) Efficiency and number of unknowns with an increasing number of uniform mesh refinements. In parenthesis, number of iterations.

P	Setup + solve (s)	# of iterations	q
128	133.0	31	2
1,024	140.4	32	8
3,456	145.5	34	16
8,192	143.8	34	32
16,000	149.6	37	64
27,648	157.1	39	128

(b) Timings of the solver. The last column provides the number of anglesets, equal to the number of *hypre* instances working concurrently.

Figure 12: weak scaling analysis of the complete solver for a system of 1.7 million unknowns per MPI process (with six reflective surfaces).

6.4. Spatial mesh refinement and weak scaling

Results were obtained on a partition of Irène composed of 2,292 nodes with two 64-core AMD Rome clocked at 2.6 GHz. The interconnect is an InfiniBand HDR full fat tree. A simple three-dimensional unstructured cube being impinged with a collimated radiative beam is now considered. It is again generated by Gmsh, with approximately 750k tetrahedra. The reflective index on the six faces of the cube is 1.5. The number of directions is now set to $N_d = 1{,}280$. This saturates the memory available on one node of Irène, so it will be used next to perform a weak scaling analysis. Inside the cube, the following coefficients are used: $(\kappa, \sigma) = (0.085, 20.10)$, as suggested in the literature [89]. After using ParMETIS to decompose this initial mesh in $128 \times i^3$ for $i \in [\![1, 6]\!]$, and assigning one subdomain per MPI rank, uniform spatial mesh refinement is performed concurrently on all processes. Each tetrahedron is split into i^3 elements, by splitting all edges of the initial elements in i. No refinement is performed for $i = 1$. The smallest problem generated for $i = 1$ has a total of 216 million unknowns, while the largest problem, running on 216 compute nodes for $i = 6$, has 45.7 billion unknowns. While the number of iterations to solve the global problem slightly increases, from 31 to 39, see third column in fig. 12b, one can notice that the overall efficiency remains above 80%, see fig. 12a. The same steps as in the previous strong scaling experiments are timed: assembly of the reference matrices $\mathcal{A}_\star$ and of the surface integrals (section 3.3), of the preconditioner B (section 4.2), preconditioner setup, and solution phase. To keep the preconditioner setup tractable, the number of anglesets q is increased with the global number of processes as shown in the rightmost column of fig. 12b. On this range of process numbers, the global preconditioner remains numerically efficient, and it converges in fewer iterates than in our previous strong scaling experiments with spherical inclusions and internal reflections, see figs. 8b and 11b for a comparison.

7. Conclusion

The radiative transfer equation is a high-dimensional integro-differential equation. In this paper, a discretization in both space and angles was used to solve it numerically. Our solver is able to discretize the RTE efficiently by using a high-level finite element language, FreeFEM. By using such a language, most of the burden inherent of the finite element method, e.g., mesh data structure, is hidden from the user. Unfortunately, these languages do not exploit the structure of the RTE and cannot be used out of the box to directly discretize it.

The mixed matrix-ready/matrix-free approach introduced in this paper has the two following important properties. First, it relies on a low number of reference matrices of a much lower dimension than the original system. These may be assembled fast using almost any domain specific language at a relatively low memory and computational cost. Second, the matrix–vector product uses a dense matrix–matrix product, which may be highly optimized, and it is possible to assemble explicitly a preconditioner to reduce the number of iterations needed by Krylov methods to converge.

By using a hybrid multigrid in space–domain decomposition in angles preconditioner, we are able to discretize and solve a 45.7 billion unknown system in less than three minutes on 27,648 MPI processes. Moreover, we show how our solver may be extended to deal with physics involving specular reflections on both exterior or interior surfaces with no orthogonality condition. Thanks to the flexibility of modern domain specific languages and

of PETSc, it would be easy to couple our solver with other fields, e.g., through a "fieldsplit" preconditioner[3]. Overall, we exhibit large-scale deterministic results on fine unstructured and arbitrarily-decomposed spatial meshes and large numbers of directions, with a mix of heterogeneous scattering, absorbing, and reflecting materials.

Acknowledgments

This work was granted access to the HPC resources of TGCC@CEA under the allocations A0050607519, A0070607519, and A0090607519 made by GENCI.

References

[1] P. J. Coelho, Advances in the discrete ordinates and finite volume methods for the solution of radiative heat transfer problems in participating media, Journal of Quantitative Spectroscopy and Radiative Transfer 145 (2014) 121–146.

[2] M. Ghattassi, J.-R. Roche, F. Asllanaj, M. Boutayeb, Galerkin method for solving combined radiative and conductive heat transfer, International Journal of Thermal Sciences 102 (2016) 122–136.

[3] P. Lesaint, P.-A. Raviart, On a finite element method for solving the neutron transport equation, Publications Mathématiques et Informatique de Rennes (1974) 1–40.

[4] E. E. Lewis, W. F. Miller, Computational methods of neutron transport, John Wiley and Sons, Inc., 1984.

[5] S. Richling, E. Meinköhn, N. Kryzhevoi, G. Kanschat, Radiative transfer with finite elements - I. Basic method and tests, Astronomy & Astrophysics 380 (2001) 776–788.

[6] E. Meinköhn, S. Richling, Radiative transfer with finite elements - II. Lyα line transfer in moving media, Astronomy & Astrophysics 392 (2002) 827–839.

[7] G. S. Abdoulaev, A. H. Hielscher, Three-dimensional optical tomography with the equation of radiative transfer, Journal of Electronic Imaging 12 (2003) 594–602.

[8] T. Tarvainen, M. Vauhkonen, S. R. Arridge, Gauss–Newton reconstruction method for optical tomography using the finite element solution of the radiative transfer equation, Journal of Quantitative Spectroscopy and Radiative Transfer 109 (2008) 2767–2778.

[9] G. Kanschat, J. C. Ragusa, A Robust Multigrid Preconditioner for S_N DG Approximation of Monochromatic, Isotropic Radiation Transport Problems, SIAM Journal on Scientific Computing 36 (2014) A2326–A2345.

[10] D. Ruh, S. Subramanian, M. Theodor, H. Zappe, A. Seifert, Radiative transport in large arteries, Biomedical Optics Express 5 (2014) 54–68.

[11] A. T. Till, J. S. Warsa, J. E. Morel, Application of linear multifrequency-grey acceleration to preconditioned Krylov iterations for thermal radiation transport, Journal of Computational Physics 372 (2018) 931–955.

[12] T. S. Haut, C. D. Ahrens, A. Jonko, R. B. Lowrie, A. T. Till, A new multigroup method for cross-sections that vary rapidly in energy, Journal of Quantitative Spectroscopy and Radiative Transfer 187 (2017) 461–471.

[13] A. G. Clements, R. Porter, A. Pranzitelli, M. Pourkashanian, Evaluation of FSK models for radiative heat transfer under oxyfuel conditions, Journal of Quantitative Spectroscopy and Radiative Transfer 151 (2015) 67–75.

[14] V. Kez, F. Liu, J.-L. Consalvi, J. Ströhle, B. Epple, A comprehensive evaluation of different radiation models in a gas turbine combustor under conditions of oxy-fuel combustion with dry recycle, Journal of Quantitative Spectroscopy and Radiative Transfer 172 (2016) 121–133.

[15] R. Viskanta, P. M. Mengüç, Radiation heat transfer in combustion systems, Progress in Energy and Combustion Science 13 (1987) 97–160.

[3] `http://www.mcs.anl.gov/petsc/petsc-current/docs/manualpages/PC/PCFIELDSPLIT.html`

[16] D. Poitou, M. El Hafi, B. Cuenot, Analysis of radiation modeling for turbulent combustion: development of a methodology to couple turbulent combustion and radiative heat transfer in LES, Journal of Heat Transfer 133 (2011).

[17] G. Kanschat, Solution of radiative transfer problems with finite elements, in: Numerical Methods in Multidimensional Radiative Transfer, Springer, 2009, pp. 49–98.

[18] T. Camminady, M. Frank, J. Kusch, Highly uniform quadrature sets for the discrete ordinates method, in: The International Conference on Mathematics and Computational Methods Applied to Nuclear Science and Engineering, 2019, pp. 25–29.

[19] C. P. Thurgood, A. Pollard, H. A. Becker, The T_N quadrature set for the discrete ordinates method, Journal of Heat Transfer 117 (1995) 1068–1070.

[20] M. A. Badri, P. Jolivet, B. Rousseau, S. Le Corre, H. Digonnet, Y. Favennec, Vectorial finite elements for solving the radiative transfer equation, Journal of Quantitative Spectroscopy and Radiative Transfer 212 (2018) 59–74.

[21] A. N. Brooks, T. J. Hughes, Streamline upwind/Petrov–Galerkin formulations for convection dominated flows with particular emphasis on the incompressible Navier–Stokes equations, Computer Methods in Applied Mechanics and Engineering 32 (1982) 199–259.

[22] M. Avila, R. Codina, J. Principe, Spatial approximation of the radiation transport equation using a subgrid-scale finite element method, Computer Methods in Applied Mechanics and Engineering 200 (2011) 425–438.

[23] J. R. Howell, M. Perlmutter, Monte Carlo solution of thermal transfer through radiant media between gray walls, Journal of Heat Transfer 86 (1964) 116–122.

[24] L. Liu, Discrete curved ray-tracing method for radiative transfer in an absorbing–emitting semitransparent slab with variable spatial refractive index, Journal of Quantitative Spectroscopy and Radiative Transfer 83 (2004) 223–228.

[25] A. Badal, F. Zafar, H. Dong, A. Badano, A real-time radiation dose monitoring system for patients and staff during interventional fluoroscopy using a GPU-accelerated Monte Carlo simulator and an automatic 3D localization system based on a depth camera, in: Physics of Medical Imaging, International Society for Optics and Photonics, 2013.

[26] M. Min, C. P. Dullemond, C. Dominik, A. de Koter, J. W. Hovenier, Radiative transfer in very optically thick circumstellar disks, Astronomy & Astrophysics 497 (2009) 155–166.

[27] R. Fournier, S. Blanco, V. Eymet, M. El Hafi, C. Spiesser, Radiative, conductive and convective heat-transfers in a single Monte Carlo algorithm, in: Journal of Physics: Conference Series, volume 676, IOP Publishing, 2016.

[28] S. Chandrasekhar, Radiative transfer, Oxford University Press (1950).

[29] H. Fujiwara, An Accurate Quadrature Rule on the Sphere for Fast Computation of the Radiative Transport Equation, arXiv:1409.0111 [math.NA] (2014).

[30] Y. Lu, A. F. Chatziioannou, A parallel adaptive finite element method for the simulation of photon migration with the radiative transfer-based model, International Journal for Numerical Methods in Biomedical Engineering 25 (2009) 751–770.

[31] G. Widmer, An efficient sparse finite element solver for the radiative transfer equation, Journal of Heat Transfer 132 (2010).

[32] D. Le Hardy, M. A. Badri, B. Rousseau, S. Chupin, D. Rochais, Y. Favennec, 3D numerical modelling of the propagation of radiative intensity through a X-ray tomographied ligament, Journal of Quantitative Spectroscopy and Radiative Transfer 194 (2017) 86–97.

[33] S. H. Kang, T.-H. Song, Finite element formulation of the first- and second-order discrete ordinates equations for radiative heat transfer calculation in three-dimensional participating media, Journal of Quantitative Spectroscopy and Radiative Transfer 109 (2008) 2094–2107.

[34] W. A. Fiveland, Discrete ordinates solutions of the radiative transport equation for rectangular enclosures, Journal of Heat Transfer 106 (1984) 699–706.

[35] M. L. Adams, E. W. Larsen, Fast iterative methods for discrete ordinates particle transport calculations, Progress in Nuclear Energy 40 (2002) 3–159.

[36] D. Mihalas, Stellar atmospheres, W. H. Freeman and Company, 1978.

[37] S. Kumar, A. Humphrey, W. Usher, S. Petruzza, B. Peterson, J. A. Schmidt, D. Harris, B. Isaac, J. Thornock, T. Harman, et al., Scalable data management of the Uintah simulation framework for next-generation engineering problems with radiation, in: Asian Conference on Supercomputing Frontiers, Springer, 2018, pp. 219–240.

[38] T. M. Evans, A. S. Stafford, R. N. Slaybaugh, K. T. Clarno, Denovo: a new three-dimensional parallel discrete ordinates code in SCALE, Nuclear Technology 171 (2010) 171–200.

[39] U. Hannebutte, P. Brown, Ardra: Scalable parallel code system to perform neutron-and radiation-transport calculations, Technical Report, Lawrence Livermore National Laboratory, 1999.

[40] M. P. Adams, M. L. Adams, W. D. Hawkins, T. Smith, L. Rauchwerger, N. M. Amato, T. S. Bailey, R. D. Falgout, Provably optimal parallel transport sweeps on regular grids, in: International Conference on Mathematics and Computational Methods Applied to Nuclear Science and Engineering, 2013.

[41] S. D. Pautz, T. S. Bailey, Parallel Deterministic Transport Sweeps of Structured and Unstructured Meshes with Overloaded Mesh Decompositions, Nuclear Science and Engineering 185 (2017) 70–77.

[42] M. P. Adams, M. L. Adams, W. D. Hawkins, T. Smith, L. Rauchwerger, N. M. Amato, T. S. Bailey, R. D. Falgout, A. Kunen, P. Brown, Provably optimal parallel transport sweeps on semi-structured grids, Journal of Computational Physics 407 (2020) 109234.

[43] S. J. Plimpton, B. Hendrickson, S. P. Burns, W. McLendon III, L. Rauchwerger, Parallel S_N sweeps on unstructured grids: algorithms for prioritization, grid partitioning, and cycle detection, Nuclear Science and Engineering 150 (2005) 267–283.

[44] F. Asllanaj, V. Feldheim, P. Lybaert, Solution of radiative heat transfer in 2D geometries by a modified finite volume method based on a cell vertex scheme using unstructured triangular meshes, Numerical Heat Transfer, Part B: Fundamentals 51 (2007) 97–119.

[45] Y. Wang, J. C. Ragusa, Diffusion synthetic acceleration for high-order discontinuous finite element S_N transport schemes and application to locally refined unstructured meshes, Nuclear Science and Engineering 166 (2010) 145–166.

[46] T. S. Haut, P. G. Maginot, V. Z. Tomov, B. S. Southworth, T. A. Brunner, T. S. Bailey, An Efficient Sweep-Based Solver for the S_N Equations on High-Order Meshes, Nuclear Science and Engineering 193 (2019) 746–759.

[47] J. I. Vermaak, J. C. Ragusa, M. L. Adams, J. E. Morel, Massively parallel transport sweeps on meshes with cyclic dependencies, Journal of Computational Physics (2020) 109892.

[48] M. Seaıd, M. Frank, A. Klar, R. Pinnau, G. Thömmes, Efficient numerical methods for radiation in gas turbines, Journal of Computational and Applied Mathematics 170 (2004) 217–239.

[49] W. F. Godoy, P. E. DesJardin, On the use of flux limiters in the discrete ordinates method for 3D radiation calculations in absorbing and scattering media, Journal of Computational Physics 229 (2010) 3189–3213.

[50] B. W. Patton, J. P. Holloway, Application of preconditioned GMRES to the numerical solution of the neutron transport equation, Annals of Nuclear Energy 29 (2002) 109–136.

[51] C. K. Krishnaprakas, K. Badari Narayana, P. Dutta, Use of GCG methods for the efficient solution of matrix problems arising from the FVM formulation of radiative transfer, Numerical Heat Transfer. Part B: Fundamentals 40 (2001) 515–533.

[52] J. P. L. Lorca, G. Kanschat, Multilevel Schwarz Preconditioners for Singularly Perturbed Symmetric Reaction–Diffusion Systems, arXiv:1811.03839 [math.NA] (2018).

[53] M. R. Charest, C. P. Groth, Ö. L. Gülder, Solution of the equation of radiative transfer using a Newton–Krylov approach and adaptive mesh refinement, Journal of Computational Physics 231 (2012) 3023–3040.

[54] B. J. Adigun, A. G. Buchan, A. Adam, S. Dargaville, M. A. Goffin, C. C. Pain, A Haar wavelet method for angularly discretising the Boltzmann transport equation, Progress in Nuclear Energy 108 (2018) 295–309.

[55] L. Soucasse, A. G. Buchan, S. Dargaville, C. C. Pain, An angular reduced order model for radiative transfer in non grey media, Journal of Quantitative Spectroscopy and Radiative Transfer 229 (2019) 23–32.

[56] G. Widmer, R. Hiptmair, C. Schwab, Sparse adaptive finite elements for radiative transfer, Journal of Computational Physics 227 (2008) 6071–6105.

[57] K. Grella, C. Schwab, Sparse tensor spherical harmonics approximation in radiative transfer, Journal of Computational Physics 230 (2011) 8452–8473.

[58] D. A. Knoll, D. E. Keyes, Jacobian-free Newton–Krylov methods: a survey of approaches and applications, Journal of Computational Physics 193 (2004) 357–397.

[59] W. F. Godoy, X. Liu, Parallel Jacobian-free Newton–Krylov solution of the discrete ordinates method with flux limiters for 3D radiative transfer, Journal of Computational Physics 231 (2012) 4257–4278.

[60] W. Bangerth, R. Hartmann, G. Kanschat, deal.II: a general-purpose object-oriented finite element library, ACM Transactions on Mathematical Software 33 (2007).

[61] A. Logg, K.-A. Mardal, G. Wells, Automated solution of differential equations by the finite element method: the FEniCS book, volume 84, Springer Science & Business Media, 2012.

[62] F. Hecht, New development in FreeFem++, Journal of Numerical Mathematics 20 (2012) 251–266.

[63] H. A. Van der Vorst, Iterative Krylov methods for large linear systems, volume 13, Cambridge University Press, 2003.

[64] S. Balay, S. Abhyankar, M. F. Adams, J. Brown, P. Brune, K. Buschelman, L. Dalcin, V. Eijkhout, W. D. Gropp, D. Kaushik, M. G. Knepley, L. C. McInnes, K. Rupp, B. F. Smith, S. Zampini, H. Zhang, PETSc web page, 2019. URL: `http://www.mcs.anl.gov/petsc`.

[65] G. Goumas, K. Kourtis, N. Anastopoulos, V. Karakasis, N. Koziris, Performance evaluation of the sparse matrix–vector multiplication on modern architectures, The Journal of Supercomputing 50 (2009) 36–77.

[66] X.-C. Cai, M. Sarkis, A restricted additive Schwarz preconditioner for general sparse linear systems, SIAM Journal on Scientific Computing 21 (1999) 792–797.

[67] K. Stüben, A review of algebraic multigrid, in: Partial Differential Equations, Elsevier, 2001, pp. 281–309.

[68] D. A. May, J. Brown, L. Le Pourhiet, A scalable, matrix-free multigrid preconditioner for finite element discretizations of heterogeneous Stokes flow, Computer Methods in Applied Mechanics and Engineering 290 (2015) 496–523.

[69] O. Axelsson, R. Blaheta, M. Neytcheva, Preconditioning of boundary value problems using elementwise Schur complements, SIAM Journal on Matrix Analysis and Applications 31 (2009) 767–789.

[70] Y. Saad, M. H. Schultz, GMRES: a generalized minimal residual algorithm for solving nonsymmetric linear systems, SIAM Journal on Scientific and Statistical Computing 7 (1986) 856–869.

[71] E. W. Larsen, Diffusion-synthetic acceleration methods for discrete-ordinates problems, Transport Theory and Statistical Physics 13 (1984) 107–126.

[72] T. S. Haut, B. S. Southworth, P. G. Maginot, V. Z. Tomov, Diffusion synthetic acceleration preconditioning for discontinuous galerkin discretizations of s_n transport on high-order curved meshes, Journal on Scientific Computing 42 (2020) B1271–B1301.

[73] V. E. Henson, U. M. Yang, *BoomerAMG*: A parallel algebraic multigrid solver and preconditioner, Applied Numerical Mathematics 41 (2002) 155–177.

[74] M. Hanuš, J. C. Ragusa, M. Hackemack, A study of various thermal upscattering acceleration schemes for massively parallel transport sweeps, in: International Conference on Mathematics & Computational Methods Applied to Nuclear Science & Engineering, 2017.

[75] M. A. Badri, Efficient finite element strategies for solving the radiative transfer equation, Ph.D. thesis, Université de Nantes, 2018.

[76] K. Kobayashi, N. Sugimura, Y. Nagaya, 3D radiation transport benchmark problems and results for simple geometries with void region, Progress in Nuclear Energy 39 (2001) 119–144.

[77] P. N. Brown, B. Chang, U. R. Hanebutte, Spherical harmonic solutions to the 3D Kobayashi benchmark suite, Technical Report, Lawrence Livermore National Laboratory, 1999.

[78] I. Zmijarevic, R. Sanchez, Deterministic solutions for 3D Kobayashi benchmarks, Progress in Nuclear Energy 39 (2001) 207–221.

[79] Y. Y. Azmy, F. X. Gallmeier, D. A. Lillie, TORT solutions for the 3D radiation transport benchmarks for simple geometries with void region, Progress in Nuclear Energy 39 (2001) 155–166.

[80] Y. Nagaya, K. Okumura, T. Mori, M. Nakagawa, MVP/GMVP 2: general purpose Monte Carlo codes for neutron and photon transport calculations based on continuous energy and multigroup methods, Technical Report, Japan Atomic Energy Research Institute, 2005.

[81] G. Karypis, V. Kumar, A fast and high quality multilevel scheme for partitioning irregular graphs, SIAM Journal on Scientific Computing 20 (1998) 359–392.

[82] R. Falgout, U. M. Yang, *hypre*: a library of high performance preconditioners, Computational Science—ICCS 2002 (2002) 632–641.

[83] A. Bienz, J. Calhoun, L. Olson, M. Snir, W. D. Gropp, Analyzing the performance of a sparse matrix vector multiply for extreme scale computers, in: The International Conference for High Performance Computing Networking, Storage, and Analysis, 2015.

[84] C. Geuzaine, J.-F. Remacle, Gmsh: a 3-D finite element mesh generator with built-in pre- and post-processing facilities, International Journal for Numerical Methods in Engineering 79 (2009) 1309–1331.

[85] G. Karypis, V. Kumar, Multilevel k-way partitioning scheme for irregular graphs, Journal of Parallel and Distributed computing 48 (1998) 96–129.

[86] L. G. Henyey, J. L. Greenstein, Diffuse radiation in the galaxy, The Astrophysical Journal 93 (1941) 70–83.

[87] G. Krishnamoorthy, R. Rawat, P. J. Smith, Parallel computations of radiative heat transfer using the discrete ordinates method, Numerical Heat Transfer 47 (2004) 19–38.

[88] D. Le Hardy, Y. Favennec, B. Rousseau, F. Hecht, Specular reflection treatment for the 3D radiative transfer equation solved with the discrete ordinates method, Journal of Computational Physics 334 (2017) 541–572.

[89] P. Yang, Q. Cheng, Z. Zhang, Radiative Properties of Ceramic Al_2O_3, AlN and Si_3N_4—II: Modeling, International Journal of Thermophysics 38 (2017) 1–18.